Direct observation of hillslope scale StorAge Selection functions in an experimental hydrologic system: Geomorphologic structure and the preferential discharge of old water

Minseok Kim [1], Till H. M. Volkmann [1,2], Yadi Wang [1,3], Ciaran J. Harman [4,5], Peter A. Troch [1,6]

[1]Biosphere 2, University of Arizona, Tucson, AZ, USA
[2]Applied Intelligence, Accenture, Kronberg im Taunus, Germany
[3]Department of Environmental Science, University of Arizona, Tucson, AZ, USA
[4]Department of Environmental Health and Engineering, Johns Hopkins University, Baltimore, MD, USA
[5]Department of Earth and Planetary Sciences, Johns Hopkins University, Baltimore, MD, USA
[6]Department of Hydrology and Atmospheric Sciences, University of Arizona, Tucson, AZ, USA

Key Points:

- We present the StorAge Selection (SAS) functions observed in a hillslope scale experimental system.
- The observed SAS functions are concave, meaning that waters flowing out are mainly older stored waters.
- Advective water dynamics and the hillslope geomorphologic structure explain the concavity.

Corresponding author: Minseok Kim, `minseok.h.kim@gmail.com`

Abstract

Spatially-integrated water transport dynamics at the hillslope scale have rarely been observed directly, and underlying physical mechanisms of those dynamics are poorly understood. We present time-variable transit time distributions (TTDs) and StorAge Selection (SAS) functions observed during a 28 days tracer experiment conducted at the Landscape Evolution Observatory (LEO), Biosphere 2, University of Arizona, AZ, USA. The observed form of the SAS functions is concave, meaning that older water in the hillslope was discharged more than younger water. The concavity is, in part, explained by the relative importance of advective and diffusive water dynamics and by the geomorphologic structure of the hillslopes. A simple numerical examination illustrates that, for straight plan shape hillslopes, the saturated zone SAS function is concave when hillslope Péclet (Pe) number is large. We also investigated the effect of hillslope planform geometry on the SAS function: The more convergent the plan shape is, the more concave the SAS function is. A numerical examination also indicates that the unsaturated zone SAS function is concave for straight and convergent hillslopes, when the soil thickness is constant. The concavity of those sub-component SAS functions signifies that the hillslope scale SAS function is concave for straight or convergent plan shape hillslopes when the hillslope Pe number is high.

1 Introduction

Field studies of hydrologic transport have been an active area of research during last decades. Numerous field sites have been studied (e.g., Sklash et al., 1986; Anderson et al., 1997; McDonnell et al., 1998; Graham et al., 2010; Gouet-Kaplan et al., 2012; Jackson et al., 2016), and those experimental studies have uncovered detailed process controls on the transport, greatly improving our process-based understanding. For example, Sklash et al. (1986) found that pre-event water generally contributes more to discharge than event water in Maimai M8 catchment, New Zealand. McDonnell et al. (1998) and Jackson et al. (2016) emphasized the importance of hydraulic conductivity variation and subsurface topographic complexity in transport dynamics. However, we still lack process-based understanding of system scale transport measures (e.g., transit time distributions) at scales useful for upscaling, such as the hillslope scale (e.g., Troch et al., 2013; Fan et al., 2019).

Looking at system scale dynamics using a spatially integrated signature has been suggested as a way forward (e.g., Klemes, 1986; Sivapalan, 2003). Such signatures would allow direct comparison of system scale dynamics across sites (Sivapalan, 2003). Also, if we understand the dominant underlying physical mechanisms of spatially-integrated signatures, the knowledge gained may be transferred across sites and spatial scales (e.g., Sivapalan, 2003; McDonnell et al., 2007). For example, hillslope scale understanding of the dynamics can serve as a building block of large scale models such as catchment scale models and Earth System Models (e.g., Troch et al., 2013; Fan et al., 2019).

Transit time distributions (TTDs) have been used widely as a spatially-integrated signature of hydrologic transport dynamics (e.g., McGuire & McDonnell, 2010; Gabrielli et al., 2018). The TTDs encapsulate spatially integrated hydrologic transport using the differences in timings between the arrival of water particles (or parcels) into a system and the discharge of those particles. However, recent research has shown that dealing with TTDs in transport modeling and mechanistically explaining TTDs is not easy (e.g., Botter et al., 2011; van der Velde et al., 2012; Ali et al., 2014; Harman, 2015; Kim et al., 2016). TTDs are time-variable under unsteady conditions (e.g., Niemi, 1977; Botter et al., 2010). There are two types of time variability: "external" and "internal" (Kim et al., 2016; Harman et al., 2016). External transport variability arises from fluctuations in incoming and outgoing fluxes, while internal transport variability describes time-varying flow paths in response to time-varying forcings (Heidbüchel et al., 2013; Kim et al., 2016). The external transport variability complicates parameterizing TTDs, and examining how system structures and flow paths are reflected in TTDs (Kim et al., 2016).

The recently developed StorAge Selection (SAS) function framework can alleviate some of these difficulties. Unlike TTDs, the SAS function does not directly explain the timing difference of inflow and outflow of water particles, but rather relates the system's internal age structure to water transit time (or age of water at the time of discharge) (Botter et al., 2011; van der Velde et al., 2012; Harman, 2015). The SAS function does not need to account for external transport variability, only internal variability (Kim et al., 2016; Harman et al., 2016; Wilusz et al., 2017; Yang et al., 2018; Kaandorp et al., 2018). (External transport variability is accounted for when the SAS function is combined with the flux time series to calculate the time-variable TTD.) The separation suggests that relating internal structure and processes to the SAS function would be easier compared to the TTDs.

However, we currently lack direct observation of the SAS functions (and TTDs) at the hillslope scale or at the catchment scale. So far, most studies have calibrated the SAS functions to reproduce the observed tracer dataset (e.g., van der Velde et al., 2014; Harman, 2015; Benettin et al., 2017; Wilusz et al., 2017; Kaandorp et al., 2018) or rely on numerical models (e.g., Danesh-Yazdi et al., 2018; Wilusz et al., 2020). While the calibrated SAS functions reproduce the tracer data set, there is no guarantee how close that function is to the actual SAS function (e.g., Harman, 2019). For example, the calibrated form may vary depending on a priori determined functional form used in a calibration procedure. This limits our ability to understand underlying physical mechanisms of the SAS function.

There is a method of directly observing the SAS functions and TTDs called PERTH (Periodic Tracer Hierarchy)(Harman & Kim, 2014). PERTH requires periodic steady state hydrodynamics which is impossible to achieve in large scale real systems. However, the Landscape Evolution Observatory (LEO) hillslopes, Biosphere 2, University of Arizona, AZ, USA, provide a unique opportunity to apply the PERTH method at the hillslope scale. The three LEO hillslopes are 330 m^3 artificial hillslopes in a controlled environment, capable of creating periodic steady state conditions. We conducted a PERTH tracer experiment for 28 days in the LEO hillslopes, yielding direct experimental observations of the SAS functions and TTDs. Here we report the results of those experiments, and use simple low-order process-based models to explain the form of the observed SAS functions. The structure of this manuscript is as follows. Section 2 provides a theoretical background on TTD and SAS functions. Section 3 describes the experimental setup and how the PERTH method was applied. In section 4, we report the experimental results, including the observed TTDs and SAS functions. In section 5, we explain the observed form of the SAS function based on physical processes. This discussion includes development of a low-order process-based model and its application to mechanistically explain the observed SAS functions.

2 Theoretical Background

We will briefly describe the essential theoretical background for the transit time distributions (TTDs) and the StorAge Selection (SAS) functions. The TTD represents hydrologic transport dynamics using the difference between the time a water particle (or parcel) enters a system and the time that the particle leave the system. The timing dif-

ference is transit time T. Two types of TTDs have been introduced: the forward TTDs (fTTDs), which describe the distribution of transit times of water that enters at an injection time t_i, and the backward TTDs (bTTDs), which describe the transit time of water that discharges at a time t. The bTTDs $\overleftarrow{p_Q}$ relate the influx concentration C_J of a conservative tracer to the outflux concentration C_Q of the tracer as (e.g., Niemi, 1977):

$$C_Q(t) = \int_{-\infty}^{t} C_J(t_i)\overleftarrow{p_Q}(t - t_i, t)dt_i \tag{1}$$

Once the bTTDs are determined, system scale conservative solute export can be modeled at a scale of interest using the equation above. However, functional form of the bTTDs are, in general, complicated under unsteady conditions, making direct application of the above equation difficult (e.g., van der Velde et al., 2014; Harman, 2015; Rinaldo et al., 2015).

The StorAge Selection (SAS) function framework provides a way to reduce these difficulties (e.g., Rinaldo et al., 2015). The framework introduces the age-ranked storage S_T (Harman, 2015) , which is the volume of water storage younger than a given age. The rank SAS function Ω_Q is the bTTDs mapped onto the age-ranked storage, that is: $\Omega_Q(S_T(T,t),t) = \overleftarrow{P_Q}(T,t) = \int_0^T p_Q(\tau,t)d\tau$. This simple mapping makes the SAS functions independent of the external variability and makes its form much simpler than TTDs. Once the SAS functions $\Omega_Q(S_T,t)$ are determined, time-evolution of the age-ranked storage can be estimated using (Harman, 2015):

$$\frac{\partial S_T(T,t)}{\partial t} = J(t) - Q(t)\Omega_Q(S_T(T,t)) - \frac{\partial S_T(T,t)}{\partial T} \tag{2}$$

The SAS function can then be converted to the bTTDs using the estimated age-ranked storage to model hydrologic transport using (1).

3 Experimental Setup

3.1 Landscape Evolution Observatory hillslopes

The tracer experiment was conducted at the Landscape Evolution Observatory (LEO) hillslopes. The three LEO hillslopes are intended to be identical artificial hillslopes located inside the glass enclosure of Biosphere 2, University of Arizona, AZ, USA (e.g., Hopp

et al., 2009; Huxman et al., 2009; Pangle et al., 2015). The three hillslopes will be referred to as LEO east, LEO center and LEO west slopes, respectively. Each 330 m^3 (30 m long, 11 m wide, and 1 m deep) hillslope has a convergent topography with an average slope of 10° (Pangle et al., 2015). Figure 1A shows a 3-D rendering of the structure. More information on the LEO hillslopes can be found elsewhere (e.g., Pangle et al., 2015; Volkmann et al., 2018), and we only provide a brief summary of the relevant information.

The steel structure is filled with basaltic tephra crushed to a loamy sand texture, except the most downslope 5.5 m^3 (0.5 m long, 11 m wide, 1 m deep; see Figure 1A) where a gravel-textured basaltic tephra is filled to facilitate lateral outflux. The average particle size fractions of the loamy sand textured crushed basaltic tephra are: 86.6% of sand (50–2000 μm), 12.2% of silt (2–50 μm), and 3.2% of clay (< 2 μm) (Pangle et al., 2015). The soil was packed layer by layer four times; 0.32 m thick wetted soil layers were added and compacted to 0.25 m thick soil layer. A terrestrial laser scanner measured the soil depth with 1 m resolution, and the measured depth is about 1 m (Pangle et al., 2015, and see Figure 1B). The soil porosity is about 0.4 (Pangle et al., 2015). The saturated soil hydraulic conductivity is about 10 m/day (which is the calibrated value in a previous modeling study of van den Heuvel et al. (2018)).

The LEO hillslopes provide a unique opportunity to conduct tracer experiments. First of all, we can control the surrounding climate. A custom-engineered irrigation system can supply water to the LEO landscapes with or without tracers. (The spatial irrigation uniformity is achieved with the coefficient of variation of 0.2 at 13 mm/hr irrigation intensity (Pangle et al., 2015).) Second, we can close the water mass balance and the tracer mass balance with high precision and high time resolution. The lateral outflow across the downslope boundary is divided into six sections, and the flow rate through each section is measured every minute with a magnetic flow meter (SeaMetrics PE102; 1 % relative error at $0.11 - 11.4$ L/min) and a tipping bucket (NovaLynx 26-2501-A). Autosamplers (customized with a single channel peristaltic pump and an Adafruit Industries stepper motor controlled by the Arduino Uno micro-controller board) collect seepage water samples at desired time intervals. An automated high-frequency (approximately 30 minutes) seepage water isotope analysis is also possible using an off-axis integrated-cavity-output spectrometer (OA-ICOS, Log Gatos Research Inc.). The automated system uses a four-channel peristaltic pump (Minipuls 3, Gilson Inc.) to deliver seepage wa-

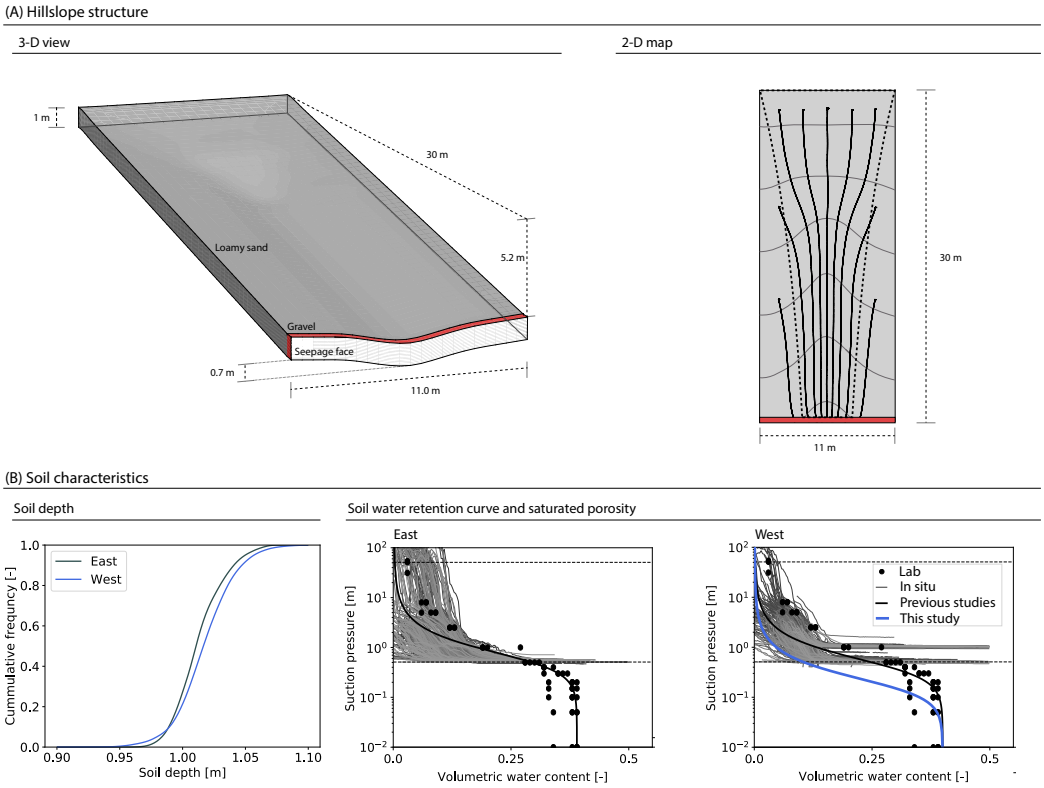

Figure 1. (A) Topological structure of the LEO hillslopes, and (B) Characteristics of the loamy sand textured soil. In the structure plots, the grey area represent loamy sand textured soil-filled area, and the red area represents the gravel-filled area. In the 2-D map, the thin solid lines are contours illustrating the elevation difference of 1 m, and the thick solid lines are hypothetical flow paths (along the steepest gradient of the steel structure). In the soil water retention curve plots, the grey lines are the in situ measurements, and the dots are the laboratory measurements. The black lines illustrate the van Genuchten curves that used in the previous numerical modeling studies of Niu et al. (2014) (for the east slope) and van den Heuvel et al. (2018) (for the west slope), and the blue line is the curve applied in this study. The dotted horizontal lines illustrate the working range of the MPS-2 sensor.

ter to a vaporization unit (Pangle et al., 2013). Thermo Scientific Dionex Ion Chromatography (DX-600), that analyze water chemistry, is also within reach. Furthermore, in order to track mass changes over time, 10 load cells (semi-custom Honeywell Model 3130) were installed under each hillslope structure.

The LEO hillslopes are also equipped with a dense internal sensor and sampling network. Soil water content is monitored at 496 locations in each hillslope using Decagon 5TM every 15 minutes. The sensors were installed at five depths—154 sensors at 0.05 m and 0.20 m depth, 76 sensors at 0.35 m depth, 78 sensors at 0.5 m depth, and 34 sensors at 0.85 m depth. 496 dielectric water potential sensors (Decagon MPS-2) are co-located with the soil water content sensors. Those sensors allow us to observe the in situ soil water retention curves (see Figure 1B). Pressure transducers (CS-451, Campbell Scientific, Inc.) were installed at 15 locations at the interface between the soil and the underlying steel structure. Assuming hydrostatic pressure, the measured pressure can be converted to water table height.

3.2 Application of the PERTH method

We adopted the PERiodic Tracer Hierarchy (PERTH) method (Harman & Kim, 2014) to estimate the TTDs and the SAS functions of the LEO hillslopes. The PERTH method enables us to directly observe the time variable TTDs and the SAS functions with a small number conservative tracers (Harman & Kim, 2014; Kim et al., 2016; Pangle et al., 2017). The essential requirement for this method is a periodic steady state (PSS) with periodic inflow, storage and outflow time series. In this experiment, a simplified version of the method described in Harman and Kim (2014) was used, and we only describe the simplified method.

Let us denote with t_C the duration of each periodic cycle, with n_C the number of periodic cycles, and with N the number of irrigation events in each periodic cycle. Following those notations, there are $n_C \times N$ irrigation events during the whole experimental period. If each pulse in the first cycle was injected with a distinct conservative tracer, we observe N breakthrough curves (BTCs) $C_i(t)$ associated with the ith irrigation pulse, where $1 \leq i \leq N$ and i is an integer. (Note that, in this study, the BTC refers the concentration breakthrough curve normalized by its injection concentration and the background concentration.) As the system is in the PSS, we can obtain the BTCs C_i asso-

ciated with the non-tracer labelled irrigation pulses $i \geq N$ by duplicating the observed BTCs as:

$$C_i(t) = C_{(i \bmod N)}(t - \lfloor i/N \rfloor t_C) \tag{3}$$

for $N < i \leq n_C \times N$, and $C_0 = C_N$.

The backward transit time distribution $\overleftarrow{p_Q}(T,t)$ during the last cycle, i.e., $t \in [(n_C - 1) \times t_C, n_C \times t_C]$ when the most information exists, can be estimated using C_i as (Harman & Kim, 2014):

$$\overleftarrow{p_Q}(t - t_i, t) = \begin{cases} \frac{C_i(t)}{\Delta_i} & \text{if } J(t_i) > 0. \\ 0 & \text{otherwise.} \end{cases} \tag{4}$$

where Δ_i is the irrigation period of the pulse i. Note that, in the above equation, t_i determines the subscript i of C_i.

The age-ranked storage density s_T, which is the age-ranked storage differentiated with respect to age T ($s_T = \partial S_T / \partial T$), can be estimated using the bTTDs:

$$s_T(t - \overline{t_i}, t) = \overline{J(t_i)} - \int_{t_i}^{t} Q(\tau) \overleftarrow{p_Q}(\tau - \overline{t_i}, \tau) d\tau \tag{5}$$

where $\bar{J}$ is the averaged irrigation rate for each irrigation event.

The SAS function $\Omega_Q(S_T(T,t)) = \overleftarrow{P_Q}(T,t)$ can then be estimated using those functions, s_T and $\overleftarrow{p_Q}$. Note that, for this experiment, evaporation was not explicitly considered, and the evaporated water was treated as if it had not entered the system. With the relatively low evaporated water volume (only about 9% or 6% of the irrigated water volume, see section 4 for details) and since young water sampling of evaporation is expected, its effect on the estimated SAS function is expected to be negligible.

We carefully designed the irrigation sequence to make as large fluctuations in storage and discharge as possible without generating overland flow. A storage-discharge relationship was used to design the irrigation sequence. The storage-discharge relationship was fitted to the dataset observed between June 1, 2016 to June 30, 2016 at the LEO

west hillslope. Based on the modeling, the sequence was determined as: $t_C = 3.5$ days with two 3 hours of 12 mm/hr irrigation events that are 7 hours apart (see Figure 2).

Deuterium (^{2}H), chloride (Cl), and bromide (Br) were selected as tracers. The Deuterium labeled water was injected with the two irrigation pulses in the first cycle, and the Cl and Br labeled water was injected with each pulse in the cycle, respectively (see Figure 2). LiCl and LiBr were used to make the Cl and Br labeled water. In terms of the symbols used in (3), the normalized BTC of Cl is C_1, and the normalized Br BTC is C_2. The normalized deuterium BTC D was used to check the quality of C_1 and C_2 using: $D = C_0 + C_1$. Injection tracer concentration of each tracer was determined similar to the previous tracer experiment conducted at the small version of the LEO hillslope (Kim et al., 2016; Pangle et al., 2017). The determined injection concentration for each tracer is: $D^* = 500$ ‰, $C_0^* = 8000$ μmol/L, and $C_1^* = 8000$ μmol/L. The actual injection concentrations are: $D^* = 521$ ‰, $C_0^* = 7988$ μmol/L, and $C_1^* = 7992$ μmol/L. We collected seepage water every hour using the custom autosamplers for water chemistry analysis. The real time isotope analysis system analyzed the deuterium enrichment of seepage water at approximately 30 minutes time interval for each slope.

4 Result

4.1 Water mass balance, periodicity, and break-through curves

The tracer experiment was conducted from December 1, 2016 to December 29, 2016. Figure 2A illustrates the time series of irrigation, discharge, storage, and the BTCs for the LEO east and the LEO west slopes. The irrigation system delivered nearly constant irrigation rate with some temporal fluctuations. We estimate the irrigation rate J based on the water mass balance using the observed discharge and the storage fluctuation; $J = Q + \Delta S/\Delta t$, where Q is the discharge rate, and $\Delta S/\Delta t$ is the storage fluctuation with $\Delta t = 1$ minute. Evaporation was assumed to be negligible during irrigation. Note that, in this paper, we do not present the results obtained at the LEO center hillslope. The center slope has a leak that accounts for about 15% of the mass-balance. The location of the leak is not yet identified, making it hard to explain the results mechanistically.

The storage S was estimated using its temporal fluctuation ($\Delta S/\Delta t$) that the load cells measured and the soil water content-based storage S_{swc} at time t_{swc}. While the SWC sensor data network is dense (496 sensors for each hillslope), the storage estimation us-

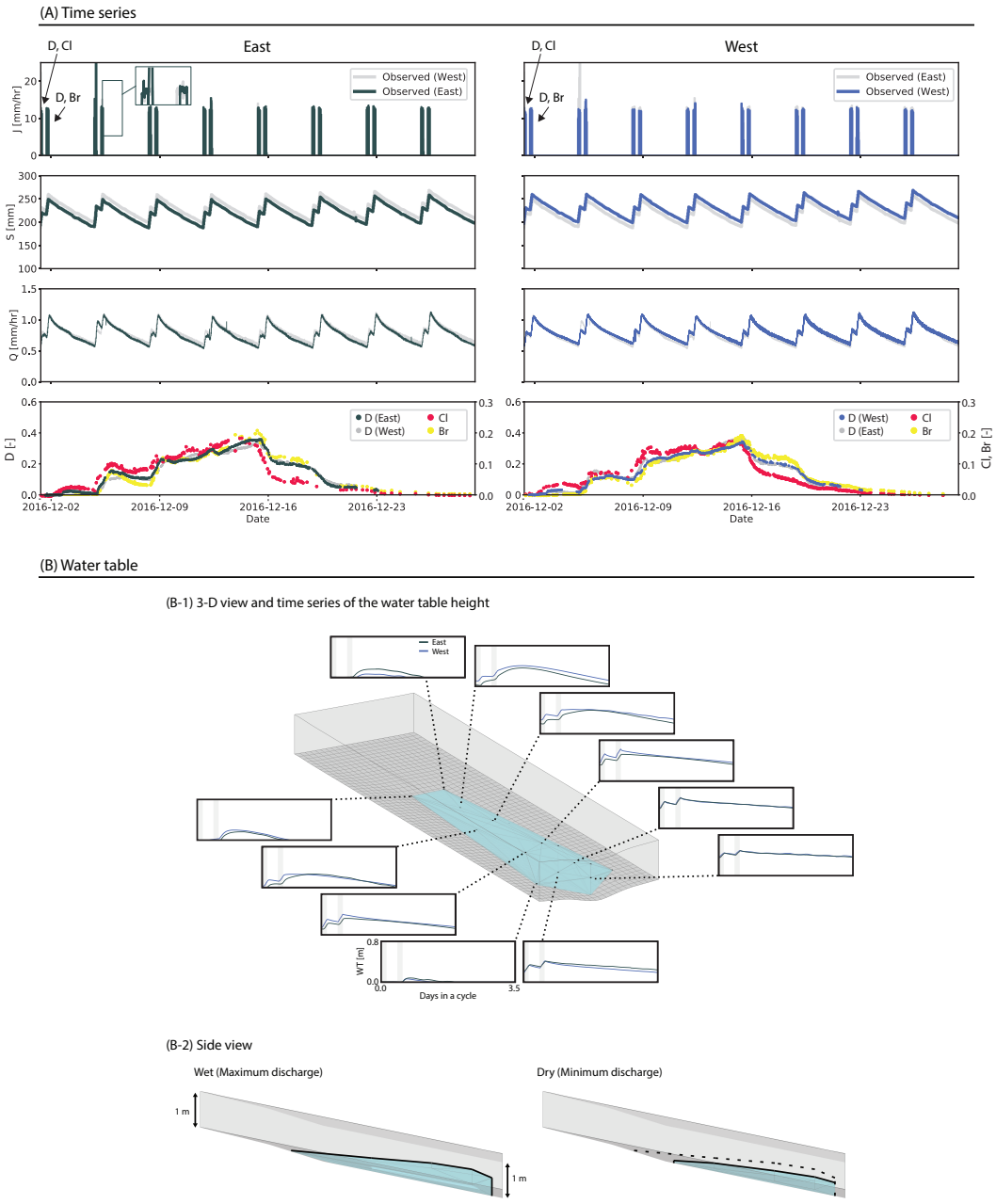

Figure 2. (A) Time series of the irrigation rate J, the total water storage S, the discharge rate Q, and the observed BTCs observed in the LEO east and the LEO west slopes. The grey lines illustrate the time series observed in the other hillslope for comparison. (B) Observed water table height and the saturated zone extent. (B1) Three-dimensional view of the LEO west hillslope saturated zone extent at the wet condition (at the maximum discharge) and the water table time series at each location in the both hillslopes. (B2) Side view of the observed water table at the wet condition and at the dry condition (at the minimum discharge). For visualization, the vertical scale is exaggerated by a factor of three. The dashed line in the side view of the dry condition figure shows the saturation zone extent at the wet condition, illustrating the water table fluctuation during the experiment.

ing the dataset required spatial interpolation and extrapolation. The nearest-neighbor method was used for both interpolation and extrapolation. t_{swc} was chosen as 8 am on January 23, 2017 when the hillslope averaged soil water content was about 0.1. The choice was to avoid overestimation since some in situ 5TM sensors overshoot at saturation (i.e., recording values exceeding soil porosity) (Gevaert et al., 2014).

The mass balance-based total irrigation amount was 564 mm and 567 mm for the LEO east and the LEO west slope, respectively. The mean irrigation intensity was 11.7 mm/hr and 11.8 mm/hr for those slopes. The total discharge amount during the experimental period was 513 mm and 532 mm, which give the runoff ratios of about 0.91 and 0.94. We estimate the evaporation amount as an unaccounted component in the mass balance, 9% and 6% for the LEO east and the LEO west slopes, respectively. The total evaporation amount was 50 mm and 34 mm, and the mean evaporation rate was 1.8 mm/day and 1.2 mm/day, respectively. Pan evaporation rate measured at the toe of those hillslopes was about 2.4 mm/day, which is higher than the estimated mean evaporation rates.

Overall, the PSS was generated reasonably well except for the second cycle in the east hillslope. During the last hour of the second pulse in the cycle, the irrigation rate was doubled due to a malfunction of the irrigation system (see the top-left panel in Figure 2). Thus, we did not irrigate water during the first hour of the following irrigation pulse, and the hillslope returned back to the PSS quickly. We examined the quality of the PSS by analyzing several observed time series using the same method that was used in Kim et al. (2016). The time series of irrigation, storage, and discharge were decomposed into three components: trend (T), periodic (P), and random (R) components. The trend component is a 3.5 days moving average of the time series. The periodic component is an average of de-trended time series over each cycle, and the random component is the remaining signal. Because of the reason described above, the second cycle of the east hillslope was excluded from this analysis. A measure similar to the signal-noise ratio, $(Var(T)+Var(R))/(Var(P)+Var(T)+Var(R))$ was used to evaluate the relative contributions of the aperiodic components to the total signal. These were 0.3% and 0.9% for the irrigation rate, 4.0% and 2.3% for the storage, and 1.8% and 2.4% for the discharge rate, respectively. These low values indicate that the trend and random part are negligible compared to the periodic part. The trend component showed that stor-

age and discharge were increased almost linearly about 10 mm and 0.03 mm/hr, respectively, throughout the experimental period, which were not significant.

The storage variation during each cycle was 60 mm around the average values of 223 mm and 230 mm for the east and west slopes, respectively. The extent of the saturated zone also changed over time. Figure 2B illustrates the PSS-averaged water table data estimated using data obtained from 15 pressure transducers by assuming hydrostatic pressure. The maximum water table fluctuation was 0.28 m and 0.27 m, respectively, at the 13 m and 7 m upslope from the seepage face. Figure 2B-1 and 2B-2 illustrate the reconstructed 3-dimensional saturated zone extent. For the 3-dimensional illustrations, Delaunay triangulation (Delaunay, 1934) was generated at each time step using a set of 3-dimensional points of the observed water table. Since no extrapolation was performed, the extent may be smaller than the actual saturated zone.

The tracer breakthrough curves (BTCs) are also illustrated in Figure 2. Thoses BTC are normalized using the tracer injection concentrations and the background concentrations. The BTCs observed at the two hillslopes are very similar. The mass recovery rates for the deuterium tracer through discharge until December 23, 12 am, 2016 are 0.88 and 0.86 for the LEO east and the LEO west slopes, respectively. The mass recovery rates for the Cl tracer until December 29, 8 am, 2016 are 0.87 and 0.90, and the rates for the Br tracer are 0.93 and 0.94, respectively.

Looking at the time series of the irrigation, the discharge, and the tracer breakthrough curves, the difference between velocity and celerity (e.g., Torres et al., 1998; McDonnell & Beven, 2014) at the hillslope scale is clear. During the entire experimental period, the hydrologic cycle controlled by celerity was repeated 7 times. However, the tracer BTCs started to increase after the first peak of the discharge and generally increased to those peaks observed in the 5th cycle. That means that the pressure wave that controls the hydrologic cycle was transmitted through the system at a much faster rate than the actual velocity that controls the propagation of tracer-labeled water. The Cl and Br BTCs are similar to the D BTC but show a little different dynamics in terms of timing. The Cl tracer BTC is the fastest among other tracer BTCs since the Cl tracer was only introduced with the first irrigation pulse. The Br BTC is the slowest, and the D BTC is in the middle.

4.2 Transit time distributions and the StorAge Selection functions

The backward TTDs and the SAS functions can be estimated using the observed BTCs and using (4) and (5). Figure 3 illustrates the estimated cumulative bTTDs and the cumulative SAS functions. The bTTDs in those hillslopes are very similar. The median transit time of the backward transit time is 11-15 days, which is comparable to the turnover time of about 11-12 days. The distributions are broadly sigmoidal, but with a staircase structure. This arises from the fact that discharged water must have arrived during irrigation periods. No water may have an age corresponding to a time in the past when the input rate J was zero. This structure is the result of external transport variability what makes TTDs difficult to parameterize and explain mechanistically in time-variable flow systems.

As described earlier, the SAS functions do not reflect the external variability directly. Indeed, the observed SAS functions in these hillslopes are much smoother than the TTDs (see Figure 3B) and reveal some features of system scale transport more directly. The observed cumulative SAS functions is concave over most of the age-ranked storage, meaning that more older water is sampled for discharge than younger.

5 Discussion

The most notable feature of the observed SAS functions is the concave shape, which indicates that older water in the hillslope is more preferentially discharged. It is not immediately clear what contributes to the observed concavity. Only few tools (or models) link the functional form of the SAS function and TTDs directly to the hillslope geomorphologic and hydraulic properties and physical process (e.g., Gelhar & Wilson, 1974; Małoszewski & Zuber, 1982; Haitjema, 1995; van der Velde et al., 2012; Ameli et al., 2016; Kim, 2018). Most of those models predict linear or convex SAS functions. In other words, they suggest hillslopes release more younger water as discharge, or release all ages in proportion to their availability in storage.

For example, Gelhar and Wilson (1974) and Haitjema (1995) showed that 2-D idealized Boussinesq-type homogeneous aquifers with non-sloping impermeable layer and nearly-horizontal recharge boundaries have an exponential TTD in the saturated zone at steady state, which corresponds with a linear (or uniform) SAS function. If one further assumes that water particles injected over the hillslope soil surface spend more or

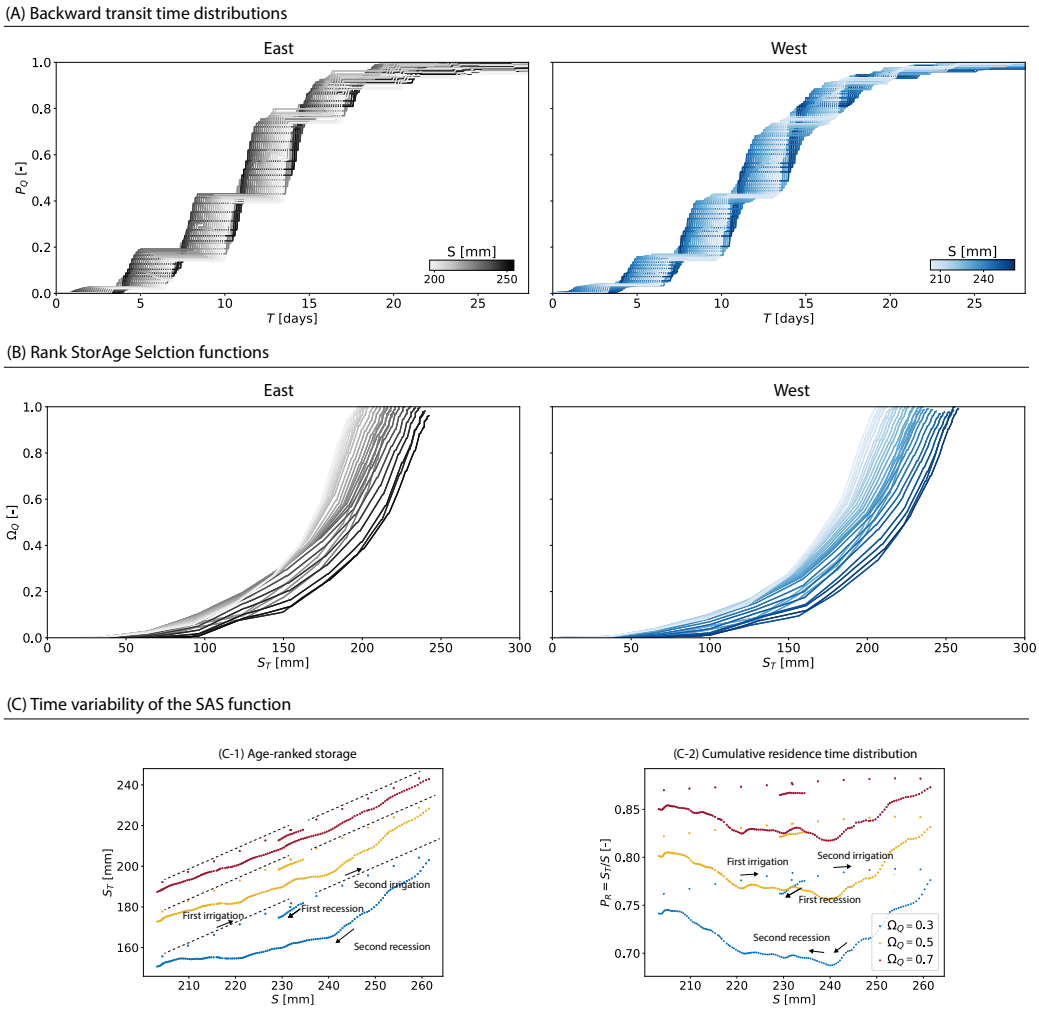

Figure 3. (A) Observed backward TTDs, (B) Observed SAS functions, and (C) LEO west SAS function time variability depending on total water storage. The bTTDs and SAS functions were plotted for every hour. Saturation of color indicates storage state from dry to wet. Panel (C) illustrates the age-ranked storage and the cumulative residence time distribution corresponding to three SAS function values: 0.3 (blue), 0.5 (yellow), and 0.7 (red). In (C-1), the dotted lines are the lines with the unit slope, approximating the observed dynamics during the irrigation periods.

less the same time in the unsaturated zone before those enter the saturated zone, one can get piston-exponential distribution as a hillslope scale TTD (Małoszewski & Zuber, 1982), which corresponds to a shifted linear SAS function. Kim (2018) showed that the linearity is due to the approximately second-order polynomial water table profile estimated by the Boussinesq equation, and in this case, the internal age structure does not vary across lateral direction (characterized as "lateral symmetry"), resulting in a linear SAS function. When the water table profile gradient gets higher downslope (and cannot be approximate by a second-order polynomial), the 2-D Boussinesq aquifer discharge is composed of more younger water, resulting in a convex-linear SAS function. The convexity is pronounced for younger age-ranked storage while the SAS function is linear over older water (Kim, 2018).

Some other models consider heterogeneous saturated hydraulic conductive structures. For example, Ameli et al. (2016) and Kim (2018) considered a decreasing saturation hydraulic conductivity with depth, while Danesh-Yazdi et al. (2018) considered stochastic hydraulic conductivity fields. These models predict linear or convex SAS functions, and convex SAS functions indicate that more younger water contributes to discharge compared to the model of Gelhar and Wilson (1974). In these models, the contribution of more younger water is because the younger water moves laterally faster along the shallower depth (because the hydraulic power is higher) or faster along the preferential flow path (determined by the stochastic hydraulic conductivity structure).

There is a notable exception where a model simulation predicts a concave SAS function. van der Velde et al. (2012) performed numerical modeling based on the Boussinesq equation to estimate the saturated zone SAS function for several ideal hillslopes of $L =$ 100 m, saturation hydraulic conductivity of 1 m/day, and downward slope depth of 1 m. A hillslope with an inclined impermeable layer (slope of 4 %) results in the concave SAS function when the steady recharge rate to the saturated area is 0.5 mm/day. The SAS function of the hillslope becomes somewhat uniform as the recharge rate increases to 1.0 mm/day. As a result, it was concluded that when the sloping aquifer storage is low, it samples more older water for discharge. However, because the result is specific to the hillslope and the condition tested, it is not clear how van der Velde et al. (2012)'s result explains the observed concavity in the LEO hillslope SAS functions. For example, it is unclear how thick the hillslope saturated layer must be and how steep the impermeable layer must be for the hillslope to drain more older water. In addition, van der Velde et

al. (2012) did not provide a process-based explanation of why the system drained more older water under those conditions. They did speculate that it might be related to the hillslope Péclet (Pe) number, a dimensionless number that explains the relative importance of the advective water dynamics to the diffusive water dynamics (Berne et al., 2005).

Inspired by van der Velde et al. (2012)'s results, we test this hypothesis and check if the hillslope Pe number helps us to better describe the observed form of the SAS function. The hillslope Pe number is a generalization of the hillslope number Hi (Brutsaert, 1994) to take into account diverse hillslope plan shapes. If hillslope plan shapes can be approximated by an exponential function $ce^{-\alpha x/L}$, where x is the horizontal coordinate and $x = 0$ at the most upslope and $x = L$ at the most downslope, the hillslope Pe number is given as: $\mathrm{Pe} = \frac{L \tan a}{2pD} - \frac{\alpha}{2}$, where L is hillslope length, a is slope angle of the impermeable layer, pD is the effective water table depth which can be estimated as a spatial average of water table height (Berne et al., 2005).

The hillslope Pe number for the LEO hillslopes was high during the experiment. A rough estimate of the hillslope Pe number is greater than 10 ($L \tan a = 5.2$ m, $2pD$ less than 0.5 m and $\alpha \approx 1.0$). It's not clear how to estimate α since the hillslopes are convergent but not exponentially. Nevertheless, the exponentially converging hillslope with $\alpha = 1.0$ can approximate the major part of the LEO hillslopes (see Figure 1A). (Note that in this case, the uncertainty due to α is small when estimating the Pe number.) The estimated high value means that the advective term in the Boussinesq equation is important. This term was not considered in the model of Gelhar and Wilson (1974) that predicts a linear SAS function.

In what follows, we adopt most of the assumptions applied in the previous models (e.g., Boussinesq-type aquifers and steady state) and investigate the effect of the sloping impervious layer and the hillslope plan shape on the hillslope scale SAS function. We also examine if the effects can be explained using the hillslope Pe number. The geometric properties of the hillslopes we consider is: the hillslope length along the datum L, the exponential width function $ce^{-\alpha x/L}$, and the slope angle of the impermeable layer a. As mentioned earlier, the exponential width function may not be suitable for describing the geomorphologic structure of the LEO hillslopes. However, rather than focusing on the detailed topography of the LEO hillslopes, we choose the exponential function to provide a more direct potential link to the previous hillslope scale theoretical studies where

the function was applied (e.g., Troch et al., 2002, 2003; Lyon & Troch, 2007; Norbiato & Borga, 2008). (Also note again that our purpose here is to investigate the origin of the concavity, not to provide a detailed model of the LEO hillslopes.)

We can use the framework developed by Kim (2018) to estimate the hillslope scale SAS function. They showed that if water particles that spend less time in the unsaturated zone also spend less time in the saturated zone, the hillslope scale SAS function can be constructed by a simple combination of the saturation zone SAS function and the unsaturated zone SAS function. Therefore, we first examine the saturated zone SAS function and the unsaturated zone SAS function separately. These SAS functions are then combined to form the hillslope scale SAS function.

5.1 Saturated zone SAS function

We first determine the saturation zone using the Boussinesq equation. The horizontal velocity field used in the Boussinesq model is then used to determine the SAS function for the saturation zone. This section briefly describes the model and details are given in Appendix A. We first look at the effect of the impermeable layer slope, and then the effect of the hillslope plan shape. In the saturated zone model, we rotate the coordinate system if the impermeable layer slope $a > 0$, so that the x axis is parallel to the impermeable layer, and "horizontal" means parallel to the layer (see Figure 4A).

The Boussinesq model is based on the Dupuit-Forchheimer assumption, which can be interpreted that total hydraulic dissipation by vertical flow is negligible (e.g., Kirkham, 1967; Haitjema, 2016). Under the assumption, vertical variation of lateral (horizontal) velocity is negligible. The assumption is generally applicable when the water level is relatively thin relative to its horizontal extent (Brutsaert, 1994). The model determines the water table, the water storage in the saturation zone, and the horizontal velocity field inside the saturation zone under steady-state. Using the lateral velocity field, we can estimate the saturated zone transit time $T_s(x)$ of water particles recharged at x using (A4), and it also allows us to estimate the TTD using (A5). Once the TTD is estimated, the age-ranked storage can be determined using the SAS function framework's governing equation (2). We can then use the TTD and the age-ranked storage to estimate the SAS function.

Using the model, a case study is firstly performed by estimating the SAS function for several cases with different hillslope Pe numbers. In this case study, the recharge rate, the saturated hydraulic conductivity, and the porosity are set to 5 mm/day, 2.5 m/day, and 0.4, respectively. The horizontal hillslope length L is set to 100 m. We set the slope of the impermeable layer to $a \in \{0.00, 0.05, 0.12, 0.15\}$ so that the Pe number varies. The boundary conditions are: no flow boundary condition at the upslope divide and the water table height $h = h_L$ at the downslope boundary. In the two high sloping cases, the downslope water table height boundary condition h_L is estimated using a kinematic-wave assumption-based model (e.g., Troch et al., 2002) which neglects the diffusive water dynamics; In other cases, it is set to 1.5 m, which is close to the kinematic-wave assumption-based model estimation for $a = 0.12$.

Figures 4A and B show the estimated water table profile, the hillslope Pe number, and the SAS function. The water level profile varies greatly depending on the hillslope Pe number. When the hillslope Pe number is zero, the water table is thicker at upslope. The total hydraulic head gradient is low at the upslope; thus water table builds up thicker at the upslope. As the hillslope Pe number increases, the thickest position moves downslope. When the hillslope Pe number is high enough (Pe ≥ 6.36 in this case study), the water table forms the wedge-like shape, which is similar to the observed water table (see Figure 2B). In that case, the lateral gradient of total hydraulic head does not vary much across the hillslope (since the advective term dominates), and the water table is getting thicker downslope as more water pass through. The estimated SAS function shows that as the hillslope Pe number increases, the SAS function becomes more concave and eventually converges to the analytical solution of the SAS function that is derived based on the kinematic-wave assumption (see Appendix B for its derivation).

In addition, 4000 simulations are performed by randomly selecting model parameters. The sampling ranges are as follows: the recharge rate $J \in [1, 20]$ mm/day, $h_L \in [0.1, 2.95]$ m, $a \in [0.0, 0.2]$, porosity $n \in [0.2, 0.6]$, and the saturated hydraulic conductivity $k \in [0.5, 5.0]$ m/day. The results indicate that as the hillslope Pe number increases, the function converges to the concave analytical solution. When Pe > 5, the Kolmogorov-Smirnov (KS) distance (the maximum vertical distance between two cumulative distributions) between the SAS function and the kinematic-wave assumption-based SAS function is less than 0.02 (see Figure 4C). The relationship between the KS distance and the hillslope Pe number is reduced to a single line, suggesting that the SAS function is pri-

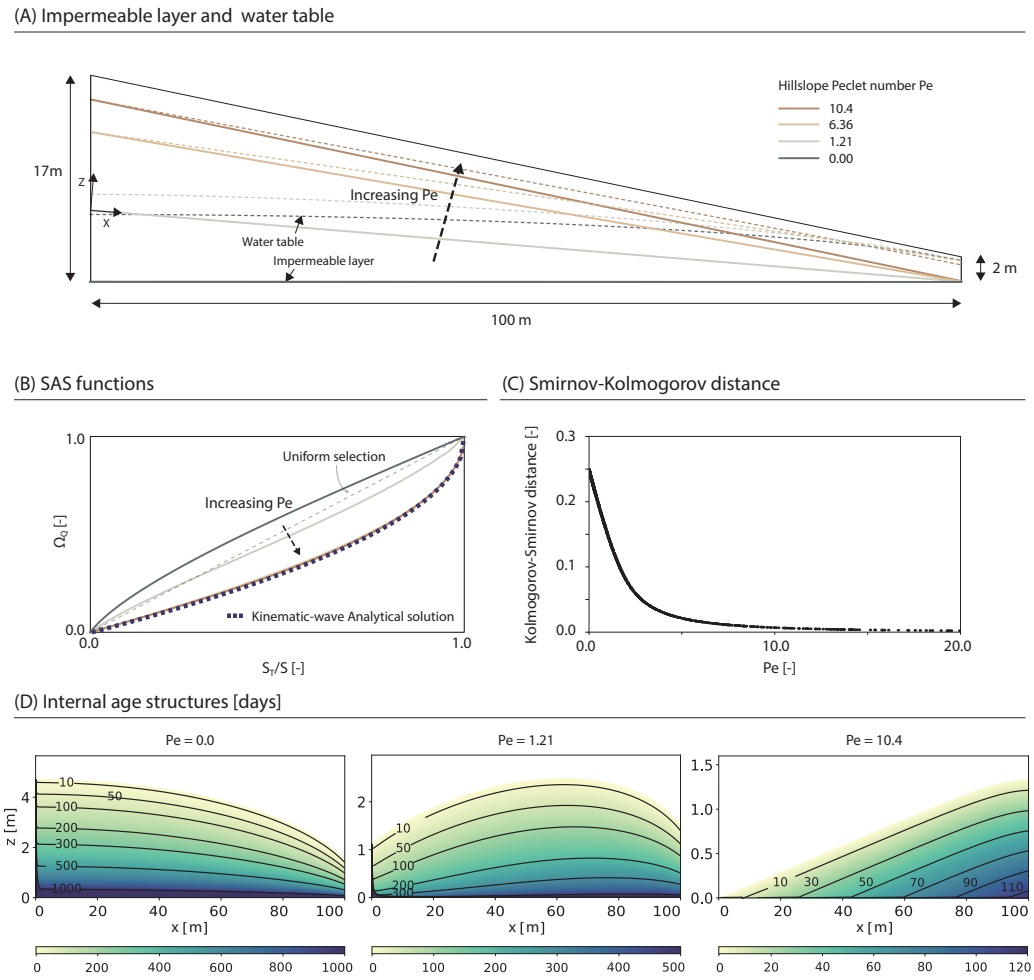

Figure 4. Water table profiles, SAS functions, and internal water age distributions for several hillslope Pe numbers. (A) Impermeable layer and water table profile, (B) SAS functions, (C) Kolmogorov-Smirnov distance between the kinematic-wave assumption-based analytical SAS function and the estimated SAS functions as a function of the hillslope Pe number, and (D) Internal water age distributions.

marily determined by the hillslope Pe number. In other words, the concavity of the SAS function can be explained by the hillslope Pe number.

Spatial water age distributions help explain the trend. Figure 4D shows the distribution of water age in the saturation zone estimated based on mass-balance (see Appendix A for details on how to estimate the spatial age distribution). When Pe is zero, the age structure is similar to the end-member case of "lateral symmetry" (Harman & Kim, 2019). As mentioned earlier, the lateral symmetry exists when the height difference between the upslope water table and the downslope water table is small and the water table profile can be approximated by a second order polynomial (Kim, 2018). The SAS function associated with the end-member case "lateral symmetry" is a linear function (uniform or random sampling) since the age distribution of the discharge is the same as the stored water age distribution. The age structure in the figure is a little different from the end-member case especially at downslope locations where the hydraulic gradient is steep. The estimated SAS function has convex form over the younger water storage and has the linear form over the older water storage (see Figure 4C). The convexity is related to the aforementioned steeper hydraulic head gradient at downslope locations; younger waters in discharge, which were injected at downslope locations, are controlled by the steeper hydraulic head gradient at the downslope locations, yielding faster lateral discharge (see Kim (2018) for more details).

In contrast, when Pe is high, old water is present only at the downslope part of the hillslope (see Figure 4D). Unlike the low Pe cases, the old water recharged at upslope went downhill due to the hydraulic head gradient similar to that of the impermeable layer gradient (the advective component). Thus, old water present only at the downslope is preferentially discharged, resulting in the concave SAS function. The age structure in this high Pe case can be characterized by "water-table parallel". Since the lateral flow velocity does not change along the horizontal direction, the contours of the age distribution move without deformation. Kim (2018) showed that the age structure is "water-table parallel" when the saturated hydraulic conductivity declines with depth fast enough so that the effect of impermeable layer on flow and transport is negligible. In that case, advective water dynamics dominate the diffusion dynamics, which is similar to the high Pe case.

However, the SAS functions in these cases are very different. In the case of decreasing hydraulic conductivity, young waters at shallower depth mobilizes faster, yielding the convex, younger water preference, SAS function (Kim, 2018). In the case of high Pe, the horizontal velocity does not change with the vertical direction, and due to the presence of a sloping impermeable layer, the old water only present around downslope, and it results in a concave SAS function. This implies that the relative importance of the advective and diffusive water dynamics is important, but understanding which process determines the relative importance (e.g., due to high Pe number or due to high Hi_X that was suggested in Kim (2018) for the declining hydraulic conductivity case) is more important in predicting the SAS function.

We also use the same model to examine the effect of the hillslope plan shape on the SAS function. For simplicity, we limit our interest to cases where the advective water dynamics dominate (i.e., when the kinematic-wave assumption holds). In this case, an analytic solution of the SAS function for the exponential width hillslopes can be derived, and the derivation steps are described in Appendix B. The analytical solutions show that the SAS function defined over the age-ranked storage normalized by the total storage (hence the fractional SAS function of van der Velde et al. (2012)) depends only on α. Figures 5A add 5B illustrate the hillslope plan shape and the associated SAS functions for several cases. The plan shapes are shown for the divergent ($\alpha = 3$), the straight ($\alpha = 0$), and the convergent ($\alpha = -3$) hillslopes, and the SAS functions are shown for $\alpha \in \{-3, -1, 0, 1, 3\}$. The results show that the more convergent the hillslope plan shape, the more concave the SAS function is (Figure 6B). As α increases, the SAS function converges to the linear function. These results indicate that the concavity of the observed SAS functions may be due in part to the convergent geometry of the LEO hillslopes.

The internal water age structures are all "water-table parallel" (see Figure 5C). Therefore, unlike the previous case, it is not easy to explain the difference in the SAS functions using the 2-D internal age structure. The more concave SAS function in the convergent hillslope is actually primarily caused by another dimension: width. In the convergent hillslope, the hillslope is wider at upslope where only younger water is present. This means that there is more younger water in the system that cannot be sampled by discharge compared to the straight hillslope and the divergent hillslope cases. It should also be noted that this trend does not coincide with the previous discussion on the hill-

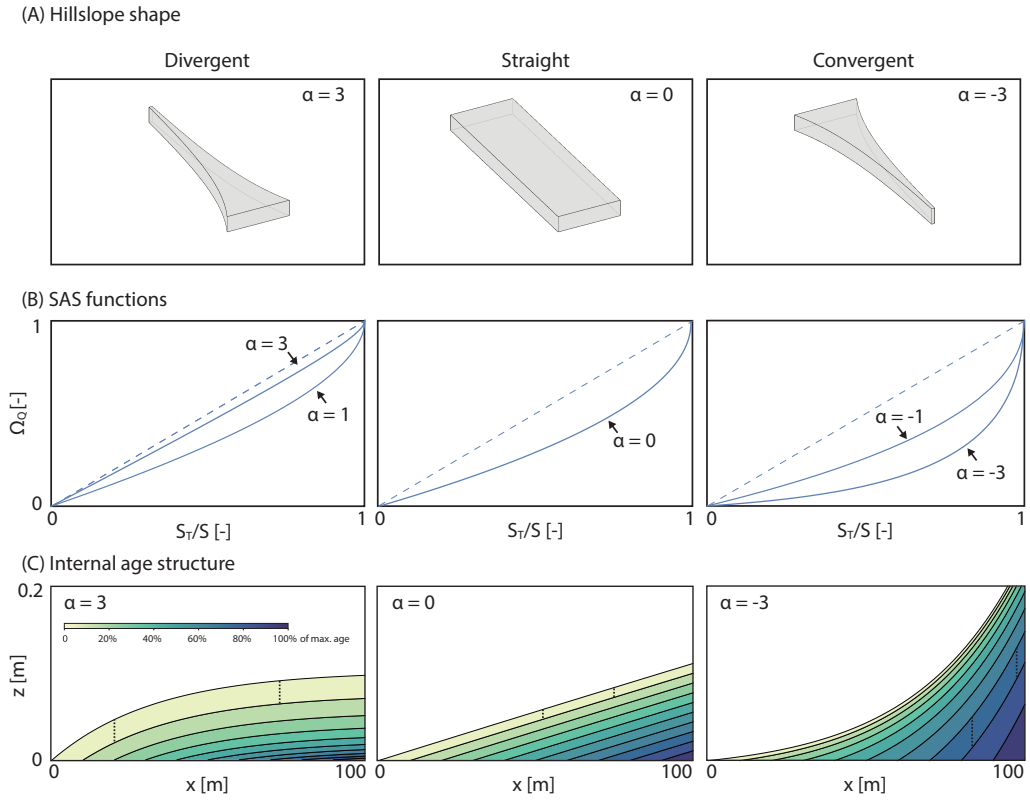

Figure 5. Hillslope plan shape, SAS function, and internal water age structure. (A) Hillslope plan shapes for $\alpha \in \{-3, 0, 3\}$. (B) Estimated SAS functions for $\alpha \in \{-3, -1, 0, 1, 3\}$. The dashed line illustrates the linear SAS function for comparison. (C) Internal water age structure. Each color represents 10% of the total age range. The two same length dotted lines in each figure indicate that the thickness of the same color region is constant, meaning that the age structure is "water-table parallel".

slope Pe number for the straight hillslopes. The hillslope Pe number decreases for more convergent hillslopes, but the SAS functions become more concave. The SAS function becomes more convex for more divergent hillslopes which eventually converges to the linear function. This is in contrast to the previously discussion for the straight hillslopes. Therefore, the hillslope Pe number alone is not sufficient for predicting the SAS function. The plan shape must also be considered.

5.2 Unsaturated zone SAS function

In estimating the unsaturated zone SAS function, we assume that water moves mostly vertically, and the unsaturated zone dynamics can be modeled as a set of one-dimensional soil columns operating independently. With this assumption, the recharge rate to the saturated zone is equal to the (steady) irrigation rate. This means that the tension saturated zone where lateral flow can occur is included in the saturation zone in this model, and the lateral flow in the tension saturated zone is treated in the same way as estimating the saturated zone lateral flow. This section briefly describes the model (see Appendix C for more information on the unsaturated zone model).

Since the LEO hillslopes are characterized with a high Pe number, we focus on the hillslope where the kinematic-wave assumption holds. It is also assumed that the soil thickness is constant, similar to the LEO hillslopes. From this section, we have set some parameters similar to the experiment: The steady irrigation rate is $J = 19$ mm/day, L = 30 m, and $a = 10°$. We estimate the unsaturated zone SAS function for three plan shapes, $\alpha = -1$, $\alpha = 0$, and $\alpha = 1$, and examine the effect of the plan shape on the SAS function.

Richard's equation can be used to estimate the one-dimensional saturation profile over the hillslope length $x \in [0, L]$ (see equation (C1)). To apply Richard's equation, we need to determine the soil-water retention curve and the relationship between suction pressure and hydraulic conductivity. The van Genuchten model was used to describe the soil-water retention characteristic, which can be written as (van Genuchten, 1980): $\theta(\psi) = \theta_r + (\theta_s - \theta_r)\left(1 + |\psi/\psi_A|^n\right)^m$ where θ is water content, θ_r is residual water content, θ_s is saturated water content, ψ is suction pressure head ($\psi < 0$), ψ_A is a parameter sometimes referred to as the air-entry pressure, n is the parameter related to the pore-size distribution, and $m = 1-1/n$. Van Genuchten-Mualem relationship (van

Genuchten, 1980) was used to describe the suction pressure head-hydraulic conductivity relationship: $k_r(\psi) = (1 + |\psi/\psi_A|^n)^{-m/2}(|\psi/\psi_A|^{-1+n}(1 + |\psi/\psi_A|^n)^{-m} - 1)^2$.

We use the parameters for those relationships determined in a previous numerical study of the LEO west hillslope, but modify one of them. van den Heuvel et al. (2018) applied a three-dimensional Richard's equation-based model to the LEO west hillslope and calibrated those parameters to reproduce the observed discharge and storage dataset. The calibrated parameters are: $\theta_s = 0.4$, $\theta_r = 0.01$, $\psi_A = 0.44$ m, and $n = 2.25$ (van den Heuvel et al., 2018). Since we assume that all lateral flows occur in the saturated zone, we reduce the extent of the tension saturated zone by changing ψ_A to 0.18 m. The modified soil-water retention curve is shown in Figure 1B with the calibrated curve in the previous study. The value was chosen so that the model's total water storage (including the saturated zone water storage) approximates the average total water storage of 228 mm observed in the LEO west slope. A numerical simulation of Kim (2018) showed that the lateral flow is negligible when $n = 2$ and $\psi_A = 0.2$ m, indicating that the lateral flow in the unsaturated zone in the model with the selected parameters is negligible.

We estimate the soil moisture content profile $\theta_u(x_i, z)$, where $i \in [1, 100]$ and x_i is uniformly distributed over $[0, L]$, by discretizing the unsaturated zone into 100 soil columns and solving the one-dimensional Richard's equation. Then, the vertical downward velocity of water particles in the unsaturated zone can be estimated as: $J/\theta_u(x_i, z)$. The unsaturated zone transit time at x_i, $T_u(x_i)$, can be estimated by integrating the inverse of velocity over the column length, which is: $S_u(x_i)/J$ (see (C2)), where $S_u(x_i)$ is the water storage in the ith column. The transit time distribution is a histogram of $T_u(x_i)$ (see (C3)), and the age-ranked storage and the SAS function can be estimated using the transit time distribution.

Figure 6A shows the estimated unsaturated zone SAS functions for the three cases ($\alpha = -1$, $\alpha = 0$, and $\alpha = 1$). The estimated SAS functions can be divided into two parts. The first part is where the SAS function is zero, and the second part is where the function is increasing. The first part exists because water must travel through some amount of unsaturated zone before it reaches the saturated zone, regardless of where the water is injected into the soil surface. Thus, the extent of the first part is related to the min-

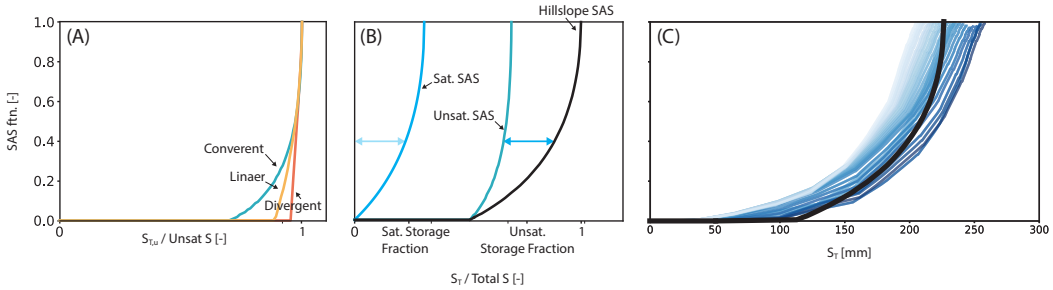

Figure 6. Sub component SAS functions and hillslope scale SAS functions. (A) Unsaturated zone SAS functions for $\alpha \in \{-1, 0, 1\}$. (B) Unsaturated zone, saturated zone, and hillslope scale SAS functions for $\alpha = -1$. The arrow lines are the same length lines, illustrating how the hillslope scale SAS function is estimated. (C) The observed SAS functions (the blue lines) and the estimated hillslope scale SAS function for $\alpha = -1$. The color saturation of the observed SAS functions illustrates the wetness condition from dry (light blue) to wet (dark blue).

imum value of $S_u(x_i)$. The extent is narrower for the convergent hillslope because water table builds up thicker in the convergent hillslope.

In the second part, the more convergent the hillslope, the more concave the SAS function. The shape of the SAS function in the unsaturated zone is largely determined by the plan shape and the water table profile. In the convergent hillslope, the SAS function becomes more concave as more water enters and exits at upslope with longer transit times. In addition, the water table profile is concave in the hillslope. Therefore, the water recharged into the saturated zone consists of a greater fraction of older water.

5.3 Hillslope scale SAS function

We can construct a hillslope scale SAS function using the saturated zone SAS function and the unsaturated zone SAS function, when both $T_u(x)$ and $T_s(x)$ decrease as x increases (Kim, 2018). The condition holds for the three cases considered in the previous section; $T_u(x)$ decreases with x since water table is thicker at downslope; $T_s(x)$ decreases with x since the flow pathway is getting shorter. When the condition is met, the hillslope scale SAS function $\Omega_Q(S_T)$ can be estimated using the inverse function of unsaturated zone SAS function $S_{T,u}(\Omega_Q)(= \Omega_Q^{-1}(S_{T,u}))$and the inverse function of the saturated zone SAS function $S_{T,s}(\Omega_Q)(= \Omega_Q^{-1}(S_{T,s}))$ as: $\Omega_Q^{-1}(S_T) = S_T(\Omega_Q) = S_{T,u}(\Omega_Q) + S_{T,s}(\Omega_Q)$ (see Appendix D and Kim (2018) for more details).

Figure 6B illustrates the saturated zone SAS function, the unsaturated zone SAS function, and the hillslope scale SAS function for the convergent hillslope with $\alpha = -1.0$. According to the model described earlier, the hillslope scale SAS function can be estimated by adding the unsaturated zone age-ranked storage and the saturated zone age-ranked storage corresponding to each value of the SAS function (see Figure 6B). The estimated hillslope scale SAS function is concave, except for the flat zero probability interval over the young age-ranked storage. The concavity of the hillslope scale SAS function is caused by the concavity of the sub component SAS functions, and the flat zero-value area is determined by the unsaturated zone SAS function. Also, we can easily expect, for the linear planar hillslope, the hillslope scale SAS function to be concave with a shift (the flat zero-value area). The function would converge to a shifted linear function when the planar shape is greatly divergent.

The similarity between the estimated hillslope scale SAS function and the observed SAS function again suggests that the observed concavity could potentially be attributed to the high hillslope Pe number and the convergent topography. The form of the estimated hillslope scale SAS function for the convergent hillslope ($\alpha = 1.0$) is close to the observed SAS function (see Figure 6C). Note again that the convergent planar shape (with $\alpha = 1.0$) is different from the LEO hillslopes, but it still approximates the major part of the LEO hillslopes (see Figure 1A).

This comparison between the observed SAS functions and the estimated SAS function shows a noteworthy difference. The observed SAS function increases earlier than the modeled SAS function, which means that the model cannot capture very young water in discharge. This may be because of the simplified unsaturated zone lateral flow and/or preferential flow pathways. In the model, lateral flow occurs at the deepest possible depth. So, if there is a smoother transition of lateral velocity along the vertical direction, the hillslope can discharge more younger water at shallower depths than the model simulates. In addition, while the soil in the hillslope is relatively homogeneous, there may still be some preferential flow paths capable of draining younger water. More detailed examination using a 3-D Richards equation model is left for future study.

5.4 Broader implications: Hypothesizing dominant controls on the SAS functions

We have shown that the observed concavity is likely due to the advection-dominated dynamics, which is inferred from the high hillslope Pe number, and the convergent topography. The basic assumption that led to the conclusion is the relative homogeneity of the soil, which made it possible to apply the process-based model using effective parameters. The soil in the hillslopes were packed with an intention to make it homogeneous (Pangle et al., 2015). Also, given that 3-D Richard's equation-based model successfully reproduced a previous experiment using the effect parameters (van den Heuvel et al., 2018), the assumption seems to be valid in these hillslopes.

The process-based understanding based on the experimental observation may help to explain real-world SAS functions that were reported in previous studies. Some studies reported the convex (at wetter condition) - concave (at drier conditions) SAS functions (van der Velde et al., 2014; Rodriguez et al., 2018; Visser et al., 2019), while some other studies reported the convex SAS functions regardless of the wetness condition (Harman, 2015; Benettin et al., 2017; Wilusz et al., 2017; Kaandorp et al., 2018).

For studies that reported the convex-concave SAS functions, the studied sites are relatively steep (Gårdsjön G1, Sweden; Marshall Gulch, AZ, USA; H. J. Andrews WS10, Oregon, USA; Southern Sierra P301, California, USA) compared to other sites where the SAS functions are convex (Lower Hafren, Wales; Tanllwyth, Wales; Springendalse, Netherlands; Roelinksbeek, Netherlands; Bruntland Burn, Scotland). If we assume that the steepness of soil-bedrock interface (or a layer that supports lateral flow during the dry periods) is not very different from the steepness of the surface topography, it can be expected that the hillslope Pe number of those steep catchments would be high because saturated zone is thin under dry conditions. Therefore, the concavity of the SAS function in dry conditions may be due in part to the high hillslope Pe number. A similar conclusion was drawn in van der Velde et al. (2014) for the Marshall Gulch and the Gårdsjön G1 catchments, where they speculated that the concavity is due to the steep topography.

Under wet condition, there are several mechanisms that can contribute to sampling more fraction of young water, so making the SAS function more convex. For example, under wet conditions, the preferential flow may be dominant over the matrix flow (e.g., Lawes et al., 1882), which results in more heterogeneous flow pathways and more frac-

tion of younger water sampling (Berghuijs & Allen, 2019; Danesh-Yazdi et al., 2018). Also, the G1 catchment is characterized with its steep exponential decline of the saturated hydraulic conductivity with depth (Nyberg, 1995). Thus, it is also possible that, under wet conditions, faster lateral flow occurs at shallow depth where hydraulic conductivity is high, resulting in more fraction of younger water sampling (e.g., Kim, 2018). Also, overland flow near a catchment outlet is another mechanism, among many others, that could result in more younger water discharge under wet conditions.

The hypothesis, relating the concavity of the catchment scale SAS functions and the high Pe number, is based on the limited number of studies. The hypothesis also has the assumption that the process-based understanding gained under steady state can account for a certain characteristic of the SAS functions under unsteady state. Nonetheless, such process-based understanding on the form of the SAS functions help us develop a hypothesis, which could be rejected with more thorough examinations at each site and with further theoretical studies under unsteady state.

Some hypotheses for the convex SAS function in humid conditions are related to soil evolution. The decrease in saturated hydraulic conductivity with depth or the preferential flow path is more pronounced in mature soil. Those hypotheses for the convex SAS function can be tested experimentally at the LEO hillslopes in future. The LEO hillslopes were built to and have been operating to observe its evolution (e.g., Pangle et al., 2015; Volkmann et al., 2018). We plan to introduce plants in the hillslopes that will accelerate its evolution, and the LEO hillslopes will allow us to track how the SAS function evolves.

5.5 On the time variability of the observed SAS functions

In this paper, we mainly focused on explaining the general form of the observed LEO hillslope SAS functions. Nevertheless, there are a few notable observations in terms of time variability of these SAS functions. For example, the "inverse storage effect", that has been extensively inferred in catchment scale studies (e.g., van der Velde et al., 2014; Harman, 2015; Wilusz et al., 2017; Benettin et al., 2017; Kaandorp et al., 2018), is not observed in these hillslopes. The inverse storage effect is the widespread observation of a larger fraction of younger water in discharge under wetter condition (Harman, 2015). The observed LEO hillslope SAS functions during the irrigation periods shift primar-

ily to the right in response to irrigated additional water entering the unsaturated zone (see Figure 3B). This means that the LEO hillslopes preferentially discharge a larger fraction of older water under wet conditions, and so seem to behave somewhat differently than what has been observed at the catchment scale elsewhere.

Figure 3C-1 shows the time variability of the LEO west SAS function with storage S. As storage S increases, the age-ranked storage corresponding to several values of Ω_Q increases, suggesting the fractions they represent are getting older. During the irrigation periods, the corresponding age-ranked storage increases nearly by the amount of storage increment (see the black dotted lines). This figure also shows hysteresis. At the same total storage, younger stored water is preferentially discharged during the recession period than during the irrigation period. Physical processes that lead to the hysteresis are not entirely clear and will be discussed in a subsequent numerical modeling study.

Figure 3C-2 is basically the same, but is plotted with the cumulative residence time distribution $P_R = S_T/S$ instead of the age-ranked storage S_T. The term "inverse storage effect" was originally introduced with the rank SAS function, that is defined over the age-ranked storage S_T, as a negative correlation between the rank SAS function scale parameter (of either a uniform or a gamma distribution) and storage. However, sometimes this term has been used with the fractional SAS function that is defined over the cumulative residence time distribution rather than the age-ranked storage (e.g., Benettin et al., 2017; Kaandorp et al., 2018). Figure 3C-2 shows mostly the same characteristics as previously described based on Figure 3C-1, but with a noteworthy difference. During the later part of the second recession period, an inverse store effect-like behavior is observed. This indicates that one should be careful when investigating the inverse storage effect because its meaning could differ depending on which SAS function is used. Nevertheless, the general dynamics shown in this figure cannot be classified as the inverse storage effect even in terms of the fractional SAS function, because the inverse storage effect is only present during a limited period.

It may seem that the LEO hillslopes are behaving differently than what has been observed in catchment scale studies, where the inverse storage effect is common. However, recent studies on the origins of the inverse storage effect suggest the LEO behavior at the hillslope scale is not inconsistent with catchment scale inverse storage effects.

Several numerical modeling studies attribute the catchment scale inverse storage effect to more diverse flow pathways or more complex soil hydraulic structure than might be in the LEO hillslopes (e.g., Wilusz et al., 2020; Pangle et al., 2017). For example, Wilusz et al. (2020) reported that their model simulated the inverse storage effect at the catchment scale in Mahantango Creek experimental catchment, PA, USA. However, individual pathways in that catchment (e.g, direct runoff, overland flow, interflow, shallow groundwater flow, and deep groundwater flow) did not show the inverse storage effect. They concluded that the modeled catchment scale inverse storage effect is due to disproportional increase in contribution from each pathway to total discharge as the catchment wets up. When the catchment is wet, it releases more water from pathways that deliver younger water. In addition, Pangle et al. (2017) reported that the inverse storage effect could be reproduced in a 2-D sloping aquifer block when saturation hydraulic conductivity deceases with depth. Such a hydraulic conductivity structure also increases the contribution from water stored at shallower depths (which is younger) to discharge as a hydrological system wets up.

6 Conclusion

We conducted a tracer experiment to observe the transit time distributions (TTDs) and the StorAge Selection (SAS) functions in the Landscape Evolution Observatory (LEO) hillslopes, Biosphere 2, University of Arizona, AZ, USA. The PERodic Tracer Hierarchy (PERTH) method was applied to observe those functions. The observed backward TTDs are similar to Gaussian distribution with the median transit time of 11 - 15 days. The observed SAS functions are concave, meaning that the hillslopes preferably discharged older water in the system.

The observed form of the SAS functions is, in part, explained by the Hillslope Péclet (Pe) number, which explains the relative controls of advective and diffusive water dynamics for homogeneous soil hillslopes. We show that, for linear planar hillslopes, as the Pe increases, the saturated zone SAS function becomes concave and converges to the kinematic wave solution of the SAS function. We also examined the effect of the hillslope planar shape on the SAS functions. A simple process-based model result shows that more convergent hillslopes discharge more older water. Also, for the hillslope with a constant soil thickness and characterized with high Pe number, the unsaturated zone SAS func-

tions show similar trend: The more convergent hillslope, the more concave SAS function. The concavity of those function results in the concave hillslope scale SAS function.

This process-based understanding help us hypothesize a process-based control on the calibrated SAS functions in other catchments. In most of the studies, the calibrated SAS functions are either convex (at wetter condition) - concave (at drier condition) or convex regardless of wetness conditions. We noticed that, for the catchment where the calibrated SAS functions are convex (wet) - concave (dry), topographic slope is higher than other catchments. It implies that the hillslope Pe number is high in those catchments at least under dry conditions, which might result in the concave SAS functions. At wetter condition, there might be other mechanisms, such as significant preferential flow, that result in the convex SAS function.

The LEO hillslopes will continue to provide exciting opportunities. Such preferential flow pathways are more pronounced in mature soil, and the LEO hillslopes were built to and have been operating to observe its evolution. Currently, the LEO hillslopes are at the beginning, the bare soil stage. We plan to introduce plants which will accelerate its evolution. Over time, the LEO hillslopes will show how the SAS functions evolve, and the result presented in this study could be used as a baseline.

Appendix A The saturated zone transport model and the SAS functions

The model domain of interest has a sloping impermeable layer with the angel a, and the saturated hydraulic conductivity is k and the soil porosity is n. We defined the 2-D coordination system as (x, z), where x is the axis parallel to the sloping impermeable layer with $x = 0$ at the most upslope, and z is the axis orthogonal to the layer with $z = 0$ at the layer. The downslope boundary is at $x = L$.

Following the (extended) Dupuit-Forcheimmer assumption, the Darcy flux $q_x(x)$ in the saturated zone is (Childs, 1971):

$$q_x(x) = -k\left(\cos a \frac{\partial h}{\partial x} - \sin a\right) \tag{A1}$$

where h is the total hydraulic head (and the water table height). The steady-state Boussinesq equation with a sloping impermeable layer, that solves water table height $h(x)$, can be written as (Childs, 1971):

$$0 = -\frac{d}{dx}(h(x)q_x(x)) + J' \tag{A2}$$

where $J' = J\cos a$ is the recharge rate which is equivalent to the irrigation rate projected onto the rotated coordinate system. This second-order differential equation requires two boundary conditions which can be written as: $q_x(0) = 0$ and $h(L) = h_L$.

The horizontal (parallel to the impermeable layer hereafter) velocity in the above model can be written as:

$$v_x(x) = -\frac{k}{n}(\cos a\frac{dh(x)}{dx} - \sin a) \tag{A3}$$

where n is porosity.

Using the horizontal velocity, we can formulate the transit time of a water particle recharged at x_0 as:

$$T_s(x_0) = \int_{x_0}^{L} \frac{1}{v_x(x')}dx', \tag{A4}$$

and the saturated zone TTD $P_{Q,s}$ is (Haitjema, 1995):

$$P_{Q,s}(T_s) = 1 - \frac{x_0(T_s)}{L} \tag{A5}$$

The age-ranked storage $S_T(T)$ can be estimated using (2) and, under steady-state, it can be simplified as:

$$S_T(T) = J'(T - \int_0^T P_{Q,s}(T')dT') \tag{A6}$$

Once the TTD $P_{Q,s}(T)$ and the age-ranked $S_T(T)$ are estimated, the SAS function can be estimated by plotting $P_{Q,s}$ as a function of S_T.

Internal water age structure can also be estimated for the Boussinesq model. We track water particles using the above model by exploiting mass-balance. Let's say we label a water particle that is recharged at x_0. When it reaches $x = x_n (> x_0)$, the water recharged above its trajectory $J'(x_n - x_0)$ should flow laterally above its vertical location $z = z_n$; thus, $J'(x_n - x_0) = q_x(x_n)(h(x_n) - z_n)$. The vertical position z_n of the particle is:

$$z_n(x_n, x_0) = \frac{J'(x_0 - x_n)}{q_x(x_n)} + h(x_n) = \frac{J(x_n - x_0)}{k(h'(x_n) - \tan a)} + h(x_n) \tag{A7}$$

The above equation can be inverted to estimate the injection location x_0 of a particle at (x, z) as: $x_0(x_n, z_n) = x_n + k(h(x_n) - z)(h'(x_n) - \tan a)/J$. It allows us to estimate the spatial age distribution $A(x, z)$ using:

$$A(x, z) = \int_{x_0(x,z)}^{x} \frac{1}{v_x(x')} dx' \tag{A8}$$

Appendix B Analytical solution of the saturated zone SAS functions under the kinematic-wave assumption

The saturated zone model can be simplified when the hillslope (Pe) number is sufficiently high (e.g., Beven, 1981; Brutsaert, 1994; Berne et al., 2005) since the diffusive water dynamic is negligible. We use the Hillslope-storage kinematic-wave model (Troch et al., 2002), which neglects the diffusive water dynamic and considers diverse hillslope plan shapes. The model assumes that transversal direction (i.e., orthogonal to both horizontal and vertical directions) gradient of total hydraulic head is negligible. With those simplifications, the lateral (horizontal) velocity (A3) becomes:

$$v_x = \frac{k}{n} \sin a, \tag{B1}$$

and the transit time $T_s(x)$ for waters recharged at x_0 is:

$$T_s(x_0) = \frac{n(L - x_0)}{k \sin a} \tag{B2}$$

When considering the plan shape, the model (A5), which determines the TTD, needs to be re-formulated. With the width function $w(x) = ce^{-\alpha x/L}$, the TTD $P_{Q,s}(T)$ can be formulated as:

$$P_{Q,s}(T_s) = 1 - \frac{1}{A}\int_0^{x_0(T_s)} w(x)dx = \frac{e^{\alpha \frac{T_s v_x}{L}} - 1}{e^{\alpha} - 1} \tag{B3}$$

where A is the area of the hillslope.

Using the $P_{Q,s}(T_s)$ and (A6), the age-ranked storage can be estimated, and the SAS function can be written as:

$$\Omega_{Q,s}(S_{T,s}) = \frac{1 + e^{\alpha} W_p\left(-e^{-\alpha - \cosh\alpha + \sinh\alpha + \frac{\alpha e^{-\alpha}(e^{\alpha}-1)v_x S_{T,s}}{J'L}}\right)}{1 - e^{\alpha}} \tag{B4}$$

where $S_{T,s}$ is the saturated zone age-ranked storage, $W_p(x)$ is the Lambert-W function with $p = \frac{\mathrm{Sgn}(x)}{2}$, and $\mathrm{Sgn}(x)$ is the sign function (Abramowitz & Stegun, 1974). The Lambert-W function is $W_p(ze^z) = z$ with $p = -1$ for $z < 0$ and $p = 0$ for $z \geq 0$ (Corless et al., 1996).

When $\alpha \to 0$, so when the plan shape is straight, the SAS function becomes:

$$\Omega_{Q,s}(S_{T,s}) = 1 - \sqrt{1 - \frac{2k\tan a}{JLn} S_{T,s}} \tag{B5}$$

In the form of the fractional SAS function $\Omega^f_{Q,s}$, which is defined over the cumulative residence time distribution $P_{R,s} = S_{T,s}/S_s$, where S_s is the saturated zone storage, those functions can be formulated as:

$$\Omega^f_{Q,s}(P_{R,s}) = \frac{1 + e^{\alpha} W_p\left(-e^{\alpha(P_{R,s}-1) + e^{-\alpha}(P_{R,s}-1) - P_{R,s}}\right)}{1 - e^{\alpha}}, \tag{B6}$$

and when $\alpha \to 0$,

$$\Omega^f_{Q,s}(P_{R,s}) = 1 - \sqrt{1 - P_{R,s}}. \tag{B7}$$

Appendix C The unsaturated zone transport model and the SAS functions

Let us denote 2-D water content field in the unsaturated zone as $\theta_u(x,z)$. If we assume that lateral flow in the unsaturated zone is negligible, the unsaturated zone water content $\theta_u(x,z)$ under the steady state can be estimated using the 1-D Richards equation:

$$0 = \frac{\partial}{\partial z}\left(k(\theta_u)\left(\frac{\partial \psi(x,z)}{\partial z} - 1\right)\right) \tag{C1}$$

where ψ is the matric head. In this study, we apply the steady flux rate J at the top soil $q = k(\frac{d\psi}{dz} - 1) = -J$ and the saturation condition at the bottom $\psi(h(x)) = 0$.

We can estimate the depth-integrated water storage in the unsaturated zone $S_u(x)$ as: $S_u(x) = \int_{h(x)}^{H(x)} \theta_u(x,z)dz$, where $H(x)$ is the soil thickness at x. Under steady state, the transit time $T_u(x)$ through the unsaturated zone can be estimated as:

$$T_u(x) = \int_{h(x)}^{H(x)} \frac{1}{v(x,z)}dz = \int_{h(x)}^{H(x)} \frac{1}{v(x,z)}dz = \frac{1}{J}\int_{h(x)}^{H(x)} \theta_u(x,z)dz = \frac{S_u(x)}{J} \tag{C2}$$

where $H(\cdot)$ is the Heaviside (or unit) step function.

The transit time distribution can be formulated as:

$$P_{Q,u}(T) = \frac{1}{L}\int_0^L H(T - T_u(x))dx = \frac{1}{L}\int_0^L H(JT - S_u(x))dx \tag{C3}$$

Using (A6), the age-ranked storage is:

$$S_{T,u}(T) = JT - \frac{1}{L}\int_0^L (JT - S_u(x))H(JT - S_u(x))dx = \frac{1}{L}\int_0^L \min(JT, S_u(x))dx, \tag{C4}$$

and the SAS function can be written as:

$$\Omega_{Q,u}(S_{T,u}) = \frac{1}{L}\int_0^L H(f^{-1}(S_{T,u}) - S_u(x))dx \tag{C5}$$

where $f(S_u(x)) = S_{T,u}$.

Appendix D The hillslope scale SAS function

We can construct the hillslope scale SAS function when there exists a monotonically increasing relationship between $T_u(x)$ and $T_s(x)$, let's say $T_s = q(T_u)$ where q is any monotonically increasing function. In that case, there exists a strictly increasing function w that satisfies $T = T_u + T_s = w(T_u)$.

The hillslope scale TTD $P_Q(T)$ can be written as:

$$P_Q(T = w(T_u)) = P_{Q,u}(w(T_u)) = P_{Q,s}(T_s = q(T_u)), \tag{D1}$$

and the age-ranked storage takes the form:

$$S_T(T) = S_{T,u}(w^{-1}(T)) + S_{T,s}(q(w^{-1}(T))) \tag{D2}$$

The above equation implies that $S_T(\Omega_Q) = S_{T,u}(\Omega_Q) + S_{T,s}(\Omega_Q)$ and that the hillslope scale SAS function is the sum of the unsaturated zone SAS function and the saturated zone SAS function if we rotate the SAS function plot counter-clockwise 90 degrees.

Acknowledgments

This work is supported by the National Science Foundation under grants EAR-1344552 and EAR-1417175. The authors gratefully acknowledge support from the Philecology Foundation of Fort Worth Texas. Additional funding support was provided by the Office of the Vice President of Research at the University of Arizona and by the Technology and Research Initiative Fund (TRIF) Water, Environmental, and Energy Solutions (WEES) initiative at the University of Arizona (Shared Equipment Enhancement Funds). Thanks to Aaron Bugaj, Nathan Abramson, Antonio Meira, Katarena Matos, John Adams, and Kimberly Land for their support during the experiment. The experimental dataset will be available at: https://biosphere2.org.

References

Abramowitz, M., & Stegun, I. A. (1974). *Handbook of Mathematical Functions,*

With Formulas, Graphs, and Mathematical Tables,. Dover Publications, Incorporated.

Ali, M., Fiori, A., & Russo, D. (2014, apr). A comparison of travel-time based catchment transport models, with application to numerical experiments. *Journal of Hydrology*, *511*, 605–618. doi: 10.1016/j.jhydrol.2014.02.010

Ameli, A., McDonnell, J. J., & Bishop, K. (2016). The exponential decline in saturated hydraulic conductivity with depth: a novel method for exploring its effect on water flow paths and transit time distribution. *Hydrological Processes*, *30*, 2438–2450. doi: 10.1002/hyp.10777

Anderson, S. P., Dietrich, W. E., Montgomery, D. R., Torres, R., Conrad, M. E., & Loague, K. (1997). Subsurface flow paths in a steep, unchanneled catchment. *Water Resources Research*, *33*(12), 2637–2653. doi: 10.1029/97WR02595

Benettin, P., Soulsby, C., Birkel, C., Tetzlaff, D., Botter, G., & Rinaldo, A. (2017). Using SAS functions and high-resolution isotope data to unravel travel time distributions in headwater catchments. *Water Resour. Res.*, *53*, 5375–5377. doi: 10.1002/2013WR014979.Reply

Berghuijs, W. R., & Allen, S. T. (2019). Waters flowing out of systems are younger than the waters stored in those same systems. *Hydrological Processes*. doi: 10.1002/hyp.13569

Berne, A., Uijlenhoet, R., & Troch, P. A. (2005). Similarity analysis of subsurface flow response of hillslopes with complex geometry. *Water Resources Research*, *41*, 1–10. doi: 10.1029/2004WR003629

Beven, K. (1981). Kinematic subsurface stormflow. *Water Resources Research*, *17*(5), 1419–1424. doi: 10.1029/WR017i005p01419

Botter, G., Bertuzzo, E., & Rinaldo, A. (2010, mar). Transport in the hydrologic response: Travel time distributions, soil moisture dynamics, and the old water paradox. *Water Resources Research*, *46*(3), 1–18. doi: 10.1029/2009WR008371

Botter, G., Bertuzzo, E., & Rinaldo, A. (2011, jun). Catchment residence and travel time distributions: The master equation. *Geophysical Research Letters*, *38*(11), L11403. doi: 10.1029/2011GL047666

Brutsaert, W. (1994). The unit response of groundwater outflow from a hillslope. *Water Resources Research*, *30*(10), 2759–2763. doi: 10.1029/94WR01396

Childs, E. (1971). Drainage of groundwater resting on a sloping bed. *Water Resources Research*, *7*(5), 1256–1263.

Corless, R. M., Gonnet, G. H., Hare, D. E. G., Jeffrey, D. J., & Knuth, D. E. (1996). On the Lambert W function. *Advances in Computational Mathematics*, *5*(1), 329–359. doi: 10.1007/BF02124750

Danesh-Yazdi, M., Klaus, J., Condon, L. E., & Maxwell, R. M. (2018). Bridging the gap between numerical solutions of travel time distributions and analytical storage selection functions. *Hydrological Processes*, *32*(8). doi: 10.1002/hyp.11481

Delaunay, B. N. (1934). Sur la sphère vide. *Bulletin of Academy of Sciences of the USSR*(6), 793–800.

Fan, Y., Clark, M., Lawrence, D. M., Swenson, S., Band, L. E., Brantley, S. L., ... Yamazaki, D. (2019). Hillslope Hydrology in Global Change Research and Earth System Modeling. *Water Resources Research*, 1737–1772. doi: 10.1029/2018WR023903

Gabrielli, C. P., Morgenstern, U., Stewart, M. K., & McDonnell, J. J. (2018). Contrasting Groundwater and Streamflow Ages at the Maimai Watershed. *Water Resources Research*, *54*. doi: 10.1029/2017WR021825

Gelhar, L. W., & Wilson, J. L. (1974). Ground-Water Quality Modeling. *Ground Water*, *12*(6), 399–408. doi: 10.1111/j.1745-6584.1974.tb03050.x

Gevaert, A. I., Teuling, A. J., Uijlenhoet, R., DeLong, S. B., Huxman, T. E., Pangle, L. A., ... Troch, P. A. (2014). Hillslope-scale experiment demonstrates the role of convergence during two-step saturation. *Hydrology and Earth System Sciences*, *18*(9), 3681–3692. doi: 10.5194/hess-18-3681-2014

Gouet-Kaplan, M., Arye, G., & Berkowitz, B. (2012). Interplay between resident and infiltrating water: Estimates from transient water flow and solute transport. *Journal of Hydrology*, *458-459*, 40–50. doi: 10.1016/j.jhydrol.2012.06.026

Graham, C. B., Woods, R. A., & McDonnell, J. J. (2010). Hillslope threshold response to rainfall: (1) A field based forensic approach. *Journal of Hydrology*, *393*(1-2), 65–76. doi: 10.1016/j.jhydrol.2009.12.015

Haitjema, H. (1995). On the residence time distribution in idealized groundwatersheds. *Journal of Hydrology*, *172*(1-4), 127–146. doi: 10.1016/0022-1694(95)02732-5

964 Haitjema, H. (2016). Horizontal Flow Models That Are Not. *Groundwater*, *54*(5),
965 613. doi: 10.1111/gwat.12448

966 Harman, C. J. (2015). Time-variable transit time distributions and transport: The-
967 ory and application to storage-dependent transport of chloride in a watershed.
968 *Water resources research*, *51*, 1–30. doi: 10.1002/2014WR015707

969 Harman, C. J. (2019). Age-Ranked Storage-Discharge Relations: A Unified Descrip-
970 tion of Spatially Lumped Flow and Water Age in Hydrologic Systems. *Water*
971 *Resources Research*, *55*(8), 7143–7165. doi: 10.1029/2017wr022304

972 Harman, C. J., & Kim, M. (2014). An efficient tracer test for time-variable tran-
973 sit time distributions in periodic hydrodynamic systems. *Geophysical Research*
974 *Letters*, 1567–1575. doi: 10.1002/2013GL058980

975 Harman, C. J., & Kim, M. (2019). A low-dimensional model of bedrock weathering
976 and lateral flow co-evolution: 1. Hydraulic theory of reactive transport. *Hydro-*
977 *logical Processes*, *33*, 466–475. doi: 10.1002/hyp.13360

978 Harman, C. J., Ward, A. S., & Ball, A. (2016). How does reach-scale stream-
979 hyporheic transport vary with discharge? Insights from rSAS analysis of se-
980 quential tracer injections in a headwater mountain stream. *Water Resources*
981 *Research*, *52*(9), 7130–7150. doi: 10.1002/2016WR018832

982 Heidbüchel, I., Troch, P. a., & Lyon, S. W. (2013). Separating physical and meteo-
983 rological controls of variable transit times in zero-order catchments. *Water Re-*
984 *sources Research*, *49*(11), 7644–7657. doi: 10.1002/2012WR013149

985 Hopp, L., Harman, C., Desilets, S., Graham, C., McDonnell, J., & Troch, P. (2009,
986 jun). Hillslope hydrology under glass: confronting fundamental questions of
987 soil-water-biota co-evolution at Biosphere 2. *Hydrology and Earth System*
988 *Sciences Discussions*, *6*(3), 4411–4448. doi: 10.5194/hessd-6-4411-2009

989 Huxman, T., Troch, P., Chorover, J., Breshears, D. D., Saleska, S., Pelletier, J., ...
990 Espeleta, J. (2009). The hills are alive: Earth science in a controlled environ-
991 ment. *Eos*, *90*(14), 120. doi: 10.1029/2009EO140003

992 Jackson, C. R., Du, E., Klaus, J., Griffiths, N. A., Bitew, M., & McDonnell,
993 J. J. (2016, aug). Interactions among hydraulic conductivity distribu-
994 tions, subsurface topography, and transport thresholds revealed by a mul-
995 titracer hillslope irrigation experiment. *Water Resources Research*. doi:
996 10.1002/2015WR018364

997 Kaandorp, V. P., Louw, P. G. B. D., van der Velde, Y., & Broers, H. P. (2018).
998 Transient groundwater travel time distributions and age-ranked storage-
999 discharge relationships of three lowland catchments. *Water Resources Re-*
1000 *search*, *48*. doi: 10.1029/2017WR022461

1001 Kim, M. (2018). *Processes and Landscape Structure Underlying System Scale Hy-*
1002 *drologic Transport: Theory, Experiment, and Modeling.* Doctoral Dissertation,
1003 Johns Hopkins University.

1004 Kim, M., Pangle, L. A., Cardoso, C., Lora, M., Volkmann, T. H., Wang, Y., ...
1005 Troch, P. A. (2016). Transit time distributions and StorAge Selection func-
1006 tions in a sloping soil lysimeter with time-varying flow paths: Direct observa-
1007 tion of internal and external transport variability. *Water Resources Research*,
1008 *52*(9). doi: 10.1002/2016WR018620

1009 Kirkham, D. (1967). Explanation of paradoxes in Dupuit-Forchheimer Seep-
1010 age Theory. *Water Resources Research*, *3*(2), 609–622. doi: 10.1029/
1011 WR003i002p00609

1012 Klemes, V. (1986). Dilettantism in Hydrology: Transition or Destiny ? *Water Re-*
1013 *sour. Res.*, *22*(9), 177–188.

1014 Lawes, J. B., Gilbert, J. H., & Warington, R. (1882). On the amount and composi-
1015 tion of the rain and drainage water collected at Rothamsted. *Journal of Royal*
1016 *Agricultural Society of England*, *18*, 1–71.

1017 Lyon, S. W., & Troch, P. A. (2007). Hillslope subsurface flow similarity: Real-
1018 world tests of the hillslope Peclet number. *Water Resources Research*, *43*(7),
1019 1–9. doi: 10.1029/2006WR005323

1020 Małoszewski, P., & Zuber, a. (1982). Determining the turnover time of ground-
1021 water systems with the aid of environmental tracers: 1. Models and their
1022 applicability. *Journal of hydrology*, *57*(3-4), 207–231. doi: 10.1016/
1023 0022-1694(82)90147-0

1024 McDonnell, J. J., & Beven, K. (2014). Debates - The future of hydrological sciences:
1025 A (common) path forward? A call to action aimed at understanding velocities,
1026 celerities and residence time distributions of the headwater hydrograph. *Water*
1027 *Resources Research*, *50*, 5342–5350. doi: 10.1002/2013WR015141

1028 McDonnell, J. J., Brammer, D., Kendall, C., Hjerdt, N., Rowe, L., Stewart, M., &
1029 Woods, R. (1998). Flow pathways on steep forested hillslopes: the tracer,

tensiometer and trough approach. *Environmental Forest Science*, *54*(1997), 463–474.

McDonnell, J. J., Sivapalan, M., Vaché, K., Dunn, S., Grant, G., Haggerty, R., ... Weiler, M. (2007, jul). Moving beyond heterogeneity and process complexity: A new vision for watershed hydrology. *Water Resources Research*, *43*(7), n/a–n/a. doi: 10.1029/2006WR005467

McGuire, K. J., & McDonnell, J. J. (2010). Hydrological connectivity of hillslopes and streams: Characteristic time scales and nonlinearities. *Water Resources Research*, *46*(10), 1–17. doi: 10.1029/2010WR009341

Niemi, A. J. (1977). Residence time distributions of variable flow processes. *The International Journal of Applied Radiation and Isotopes*, *28*, 855–860.

Niu, G. Y., Pasetto, D., Scudeler, C., Paniconi, C., Putti, M., Troch, P. a., ... Zeng, X. (2014). Incipient subsurface heterogeneity and its effect on overland flow generation - Insight from a modeling study of the first experiment at the Biosphere 2 Landscape Evolution Observatory. *Hydrology and Earth System Sciences*, *18*(5), 1873–1883. doi: 10.5194/hess-18-1873-2014

Norbiato, D., & Borga, M. (2008). Analysis of hysteretic behaviour of a hillslope-storage kinematic wave model for subsurface flow. *Advances in Water Resources*, *31*(1), 118–131. doi: 10.1016/j.advwatres.2007.07.001

Nyberg, L. (1995). Water flow path interactions with soil hydraulic properties in till soil at Gårdsjön, Sweden. *Journal of Hydrology*, *170*(1-4), 255–275. doi: 10.1016/0022-1694(94)02667-Z

Pangle, L. A., DeLong, S. B., Abramson, N., Adams, J., Barron-Gafford, G. A., Breshears, D. D., ... Zeng, X. (2015). The Landscape Evolution Observatory: A large-scale controllable infrastructure to study coupled Earth-surface processes. *Geomorphology*(August). doi: 10.1016/j.geomorph.2015.01.020

Pangle, L. A., Kim, M., Cardoso, C., Lora, M., Meira Neto, A. A., Volkmann, T. H., ... Harman, C. J. (2017). The mechanistic basis for storage-dependent age distributions of water discharged from an experimental hillslope. *Water Resources Research*, *53*, 2733–2754. doi: 10.1002/2016WR019901

Pangle, L. A., Klaus, J., Berman, E. S. F., Gupta, M., & McDonnell, J. J. (2013). A new multisource and high-frequency approach to measuring δ2H and δ18O in hydrological field studies. *Water Resources Research*, *49*(11), 7797–7803. doi:

10.1002/2013WR013743

Rinaldo, A., Benettin, P., Harman, C. J., Hrachowitz, M., Mcguire, K. J., Velde, Y. V. D., ... Botter, G. (2015). Storage selection functions: A coherent framework for quantifying how catchments store and release water and solutes. *Water Resourses Research*, *51*, 1–8. doi: 10.1002/2015WR017273

Rodriguez, N. B., McGuire, K. J., & Klaus, J. (2018). Time-Varying Storage – Water Age Relationships in a Catchment with a Mediterranean Climate. *Water Resources Research*, *0*(ja). doi: 10.1029/2017WR021964

Sivapalan, M. (2003). Process complexity at hillslope scale, process simplicity at the watershed scale: is there a connection? *Hydrological Processes*, *17*(5), 1037–1041. doi: 10.1002/hyp.5109

Sklash, M., Stewart, M., & Pearce, A. (1986). Storm Runoff Generation in Humid Headwater Catchments: 2. A Case Study of Hillslope and Low-Order Stream Response. *Water Resources Research*, *22*(8), 1273–1282.

Torres, R., Dietrich, W. E., Montgomery, D. R., Anderson, S. P., & Loague, K. (1998, aug). Unsaturated zone processes and the hydrologic response of a steep, unchanneled catchment. *Water Resources Research*, *34*(8), 1865–1879. doi: 10.1029/98WR01140

Troch, P. A., Berne, A., Bogaart, P., Harman, C., Hilberts, A. G. J., Lyon, S. W., ... Verhoest, N. E. C. (2013). The importance of hydraulic groundwater theory in catchment hydrology: The legacy of Wilfried Brutsaert and Jean-Yves Parlange. *Water Resources Research*, *49*(9), 5099–5116. doi: 10.1002/wrcr.20407

Troch, P. A., Paniconi, C., & Emiel van Loon, E. (2003). Hillslope-storage Boussinesq model for subsurface flow and variable source areas along complex hillslopes: 1. Formulation and characteristic response. *Water Resources Research*, *39*(11). doi: 10.1029/2002WR001728

Troch, P. A., Van Loon, E., & Hilberts, A. (2002). Analytical solutions to a hillslope-storage kinematic wave equation for subsurface flow. *Advances in Water Resources*, *25*(6), 637–649. doi: 10.1016/S0309-1708(02)00017-9

van den Heuvel, D., Troch, P., Booij, M., Niu, G., Volkmann, T., & Pangle, L. (2018). Effects of differential hillslope-scale water retention characteristics on rainfall-runoff response at the Landscape Evolution Observatory. *Hydrological*

Processes(December 2017), 1–10. doi: 10.1002/hyp.13148

van der Velde, Y., Heidbüchel, I., Lyon, S. W., Nyberg, L., Rodhe, A., Bishop, K., & Troch, P. a. (2014). Consequences of mixing assumptions for time-variable travel time distributions. *Hydrological Processes*. doi: 10.1002/hyp.10372

van der Velde, Y., Torfs, P. J. J. F., van der Zee, S. E. a. T. M., & Uijlenhoet, R. (2012, jun). Quantifying catchment-scale mixing and its effect on time-varying travel time distributions. *Water Resources Research*, *48*(6), W06536. doi: 10.1029/2011WR011310

van Genuchten, M. T. (1980). A Closed-form Equation for Predicting the Hydraulic Conductivity of Unsaturated Soils. *Soil Science Society of America Journal*, *44*(5), 892. doi: 10.2136/sssaj1980.03615995004400050002x

Visser, A., Thaw, M., Deinhart, A., Bibby, R., Safeeq, M., Conklin, M., ... Van der Velde, Y. (2019). Cosmogenic Isotopes Unravel the Hydrochronology and Water Storage Dynamics of the Southern Sierra Critical Zone. *Water Resources Research*. doi: 10.1029/2018WR023665

Volkmann, T. H. M., Sengupta, A., Pangle, L. A., Dontsova, K., Barron-Gafford, G. A., Harman, C. J., ... Troch, P. A. (2018). Controlled Experiments of Hillslope Coevolution at the Biosphere 2 Landscape Evolution Observatory: Toward Prediction of Coupled Hydrological, Biogeochemical, and Ecological Change. In J. Liu & W. Gu (Eds.), *Hydrology of artificial and controlled experiments* (chap. 2). London, UK: InTech. doi: 10.5772/intechopen.72325

Wilusz, D. C., Harman, C. J., & Ball, W. P. (2017). Sensitivity of Catchment Transit Times to Rainfall Variability Under Present and Future Climates. *Water Resources Research*, *53*(12), 10231–10256. doi: 10.1002/2017WR020894

Wilusz, D. C., Harman, C. J., Ball, W. P., Maxwell, R. M., & Buda, A. R. (2020). Using Particle Tracking to Understand Flow Paths, Age Distributions, and the Paradoxical Origins of the Inverse Storage Effect in an Experimental Catchment. *Water Resources Research*, *56*(4), e2019WR025140. doi: 10.1029/2019WR025140

Yang, J., Heidbüchel, I., Musolff, A., Reinstorf, F., & Fleckenstein, J. H. (2018). Exploring the Dynamics of Transit Times and Subsurface Mixing in a Small Agricultural Catchment. *Water Resources Research*, *54*(3), 2317–2335. doi: 10.1002/2017WR021896